



Production of syngas with controllable H₂/CO ratio by high temperature co-electrolysis of CO₂ and H₂O over Ni and Co- doped lanthanum strontium ferrite perovskite cathodes

Dhruba J. Deka^a, Seval Gunduz^a, Taylor Fitzgerald^a, Jeffrey T. Miller^b, Anne C. Co^c, Umit S. Ozkan^{a,*}

^a William G. Lowrie Department of Chemical and Biomolecular Engineering, The Ohio State University, Columbus, OH 43210, USA

^b Davidson School of Chemical Engineering, Purdue University, West Lafayette, IN 47907, USA

^c Department of Chemistry and Biochemistry, The Ohio State University, Columbus, OH 43210, USA

ARTICLE INFO

Keywords:

Perovskite oxide
Solid oxide electrolysis cell
High-temperature co-electrolysis
Syngas production
H₂/CO ratio
In-situ XANES

ABSTRACT

Conversion of CO₂ and H₂O into synthesis gas (a mixture of H₂ and CO) in a high temperature solid oxide electrolysis cell (SOEC) is an attractive route for CO₂ utilization. Depending on the composition of the syngas, it can be directly used as a fuel or fed to an oxo process or a Fischer-Tropsch process to produce value added chemicals. Designing an efficient and stable cathode for an SOEC that can yield syngas with controllable H₂/CO ratio is of fundamental interest. In the current study, Ni and Co- doped A-site deficient perovskite materials of the form La_{0.7}Sr_{0.2}Ni_xCo_yFe_{1-x-y}O₃ (x, y = 0; x = 0, y = 0.2; x = 0.1, y = 0.1; x = 0.2, y = 0) are studied as SOEC cathodes for co-electrolysis of CO₂ and H₂O at 800 °C. Modifications of the surface and bulk properties of these materials due to doping were investigated using in-situ XRD, XPS, Raman spectroscopy, electronic conductivity measurements, oxygen mobility test, in-situ DRIFTS and XANES. The Co- doped perovskite La_{0.7}Sr_{0.2}Co_{0.2}Fe_{0.8}O₃ showed the lowest Faradaic efficiency and the ones doped with Ni showed nearly 100% Faradaic efficiency for total production of H₂ and CO where the H₂/CO ratio in the produced syngas increased with increasing Ni content in the cathode material. This ratio could be controlled by tuning the B-site dopant levels, cell voltage and H₂O/CO₂ ratio in the cathode feed stream. In-situ XANES studies showed that during CO₂ and H₂O co-electrolysis, the Co ions in La_{0.7}Sr_{0.2}Co_{0.2}Fe_{0.8}O₃ may get oxidized, thus possibly reducing the number of oxygen vacancies in the material and hence lowering the electrochemical activity. Moreover, post-electrolysis analyses show that the Co- doped cathode forms graphitic carbon, which lowers the Faradaic efficiency for syngas production. No graphitic carbon formation was observed on the Ni- doped cathodes. A long-term co-electrolysis test performed for approximately 110 h on a La_{0.7}Sr_{0.2}Ni_{0.1}Co_{0.1}Fe_{0.8}O₃ cathode shows good stability of these materials in terms of electrochemical performance and coke resistance.

1. Introduction

The global average CO₂ level in the atmosphere is over 400 ppm and is still rising at an alarming rate [1]. Curtailing the emission of this greenhouse gas is becoming a major goal for both the policymakers and scientists. An effective way to achieve this feat is to convert CO₂ into value added chemicals instead of releasing it to the atmosphere [2]. High temperature solid oxide electrolysis cell (SOEC) is a promising technology that can efficiently split CO₂ to form CO and O₂ [3,4]. In fact, recent focus has been to electrolyze both CO₂ and H₂O simultaneously in an SOEC to produce a mixture of CO and H₂ which is also called as synthesis gas [5–37]. This mixture can be used as a fuel and

feed to an oxo or Fischer-Tropsch synthesis process where value-added chemicals are catalytically produced from H₂ and CO. Moreover, pure oxygen gas is obtained as a secondary product from these electrolyzers. While conventional methods of syngas production such as steam reforming of hydrocarbons and coal gasification form CO₂ as a side product, high temperature electrolysis can in fact consume CO₂ to produce syngas. High-temperature electrolysis is economically more attractive than low-temperature electrolysis because the electricity demand is lower and less expensive catalytic materials can be used at high temperatures [10,34,38].

In an SOEC, CO₂ and H₂O molecules are electrolyzed at the cathode resulting in the formation of CO, H₂ and O²⁻ ions. These O²⁻ ions

* Corresponding author.

E-mail address: ozkan.1@osu.edu (U.S. Ozkan).

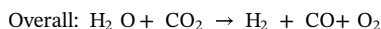
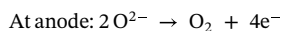
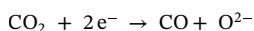
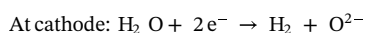
<https://doi.org/10.1016/j.apcatb.2019.02.045>

Received 13 November 2018; Received in revised form 18 January 2019; Accepted 16 February 2019

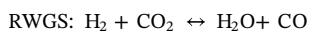
Available online 19 February 2019

0926-3373/ © 2019 Elsevier B.V. All rights reserved.

move through the dense solid oxide electrolyte to the anode where they combine to form molecular oxygen. The associated half reactions are shown below:



Studies have shown that the reverse water gas shift (RWGS) reaction can also be involved during high temperature co-electrolysis [7,23,39–41].



Designing the cathode material of an SOEC is a challenging task. The materials used for this purpose should have properties including, but not limited to, high ionic and electronic conductivity, stability at high temperature under the complex reaction environment, resistance towards coke formation, comparable thermal expansion properties with the electrolyte material [32,33]. The most widely studied cathode material for CO_2 and H_2O co-electrolysis is Ni-YSZ cermet (YSZ = Yttria-stabilized Zirconia) [7,11,23,30,33,34]. In this material, Ni particles provide electronic conductivity whereas the YSZ matrix provides oxygen ion conductivity. Electrochemical reactions take place at the interface of Ni and YSZ exposed to reactant gas, also known as the three-phase boundary (TPB). Even though high co-electrolysis activity of Ni-YSZ has been reported by various studies, this material suffers degradation under SOEC environment. Oxidation of Ni into insulating NiO phase, formation of zirconium oxide phase around Ni-particles, agglomeration of Ni particles, coke formation (Ni is an excellent catalyst for the Boudouard reaction, $2\text{CO} \rightleftharpoons \text{CO}_2 + \text{C}$) are some of the various problems associated with Ni-YSZ cathode [29,33,34]. Moreover, since Ni gets oxidized at the high operating temperature under the oxidizing environment provided by CO_2 and H_2O , a “safe gas” (a gas that maintains an overall reducing environment) such as H_2 or CO needs to be added to the cathode feed to keep Ni in the metallic state, and that adds to the process economy. All these issues encouraged researchers to search for alternative cathode materials.

Mixed metal oxides with perovskite crystal structure have gained attention in recent years as cathode materials for high temperature co-electrolysis of CO_2 and H_2O [6,14,19,20,22,27,29,31,41]. The general chemical formula of a perovskite oxide is ABO_3 , where A is an alkali or alkaline earth metal ion and B is a transition metal ion. In an ideal cubic perovskite, B is octahedrally coordinated to six oxygen atoms while A is coordinated to twelve oxygen atoms [42–44]. Perovskites can have both ionic and electronic conductivity, thus extending the TPB to the bulk of the material. Moreover, with rational doping of the A or B-site, these transport properties can be enhanced, and electrochemical activity of the material can be tuned. Perovskite oxides can also be used without the presence of a safe gas, have stability under the SOEC reaction environment and are resistant to coke formation. $\text{La}_{0.7}\text{Sr}_{0.25}\text{Cr}_{0.5}\text{Mn}_{0.5}\text{O}_3$, $\text{La}_{0.2}\text{Sr}_{0.8}\text{TiO}_3$, $\text{La}_{0.7}\text{Sr}_{0.3}\text{V}_{0.9}\text{O}_4$, $\text{La}_{0.6}\text{Sr}_{0.4}\text{Mn}_{0.2}\text{Fe}_{0.8}\text{O}_{3.8}$, $\text{Sr}_2\text{Fe}_{1.5}\text{Mo}_{0.5}\text{O}_{6.8}$, $\text{Sm}_{0.5}\text{Sr}_{0.5}\text{CoO}_{3.8}$ are some of the perovskite oxides that has been studied as a cathode for co-electrolysis operation [6,14,19,20,22,27,29,31,36,37,41]. These studies are primarily focused on electrochemical performance of the perovskite cathode in terms of cell voltage, current density and polarization resistance. From catalysis point of view, a systematic study of the surface-reactant interaction, role of A or B-site metal ions during electrolysis and stability under long-term operation is still needed on these materials before a ready-to-commercialize cathode can be found.

One important aspect that could decide the commercial feasibility of a high temperature co-electrolysis process is the composition of the product syngas. Different H_2/CO ratios are required for the synthesis of different chemicals. For example, a H_2/CO ratio of 2 is desired for F–T syntheses, whereas a H_2/CO ratio of 1 is needed for production of

aldehydes by hydroformylation or the oxo process [45]. Natural gas-based plants typically produce syngas too rich in hydrogen and thus needs a downstream process such as the pressure swing absorption (PSA) unit to adjust the H_2/CO ratio which adds to the operating and the maintenance cost. High temperature co-electrolysis of H_2O and CO_2 could give an opportunity to perform both the production of syngas and the control of its composition in one step. H_2/CO ratio of the syngas produced by co-electrolysis can depend on various parameters such as cell voltage, $\text{H}_2\text{O}/\text{CO}_2$ ratio in the cathode feed, temperature and the cathode material properties. Even though much work has been done on synthesizing new cathode materials and designing efficient cell stacks, only a few studies have addressed the issue of product distribution. Further studies are needed for making this technology economically viable. Nevertheless, an economic analysis performed by Graves et al. [10] shows that with a wholesale electricity price of 4–5 U.S. cents/kWh, gasoline produced with the currently available high-temperature electrolysis technology combined with Fischer-Tropsch synthesis would cost approximately \$ 3/gallon. Thus, with certain improvement in the electrode materials, cell design and product syngas quality, synthetic fuel produced based on high-temperature electrolysis technology could become economically competitive with conventional fossil fuel-based technologies.

In the current study, performance of an A-site deficient perovskite oxide, $\text{La}_{0.7}\text{Sr}_{0.2}\text{FeO}_3$, as a co-electrolysis cathode catalyst without the use of a safe gas is investigated. Significant enhancement of the electrochemical activity is seen by doping the Fe-site of this material with Ni or both Ni and Co, with the Faradaic efficiency reaching as high as 100% for the doped cathodes. The H_2/CO ratio of the produced syngas can be controlled by tuning the dopant levels. The surface and bulk properties of the catalysts are probed with XRD, XPS, XANES, conductivity measurement, Raman spectroscopy and temperature-programmed experiments. In order to understand the behavior of a catalyst during a reaction, it is important to perform the characterization tests in-situ. Here, an in-situ XANES study of the cathode catalysts under co-electrolysis conditions is reported to elucidate the differences in the behavior of these materials during reaction.

2. Experimental section

2.1. Catalyst synthesis

An EDTA-citric acid complexation route was used for synthesizing doped lanthanum ferrite catalysts. In this method, stoichiometric amounts of $\text{La}(\text{NO}_3)_3 \cdot 6\text{H}_2\text{O}$, $\text{Sr}(\text{NO}_3)_2$, $\text{Ni}(\text{NO}_3)_2 \cdot 6\text{H}_2\text{O}$, $\text{Co}(\text{NO}_3)_2 \cdot 6\text{H}_2\text{O}$ and $\text{Fe}(\text{NO}_3)_3 \cdot 9\text{H}_2\text{O}$ were first dissolved in deionized water. EDTA in a stoichiometric ratio of 1.5:1 with respect to the metal ions was then added to this solution under uniform stirring and heating. Citric acid was added when the solution reached a temperature of 60 °C, followed by dropwise addition of NH_4OH to adjust the pH to 6. The complex solution prepared this way was then kept at 90 °C under constant stirring. Once the solvent evaporated, a gel was formed which was then dried at 150 °C for 12 h to obtain a black amorphous material. This powder was calcined at 1000 °C for 5 h to obtain powdered perovskite oxide samples. The different compositions of samples synthesized for this study are: $\text{La}_{0.7}\text{Sr}_{0.2}\text{FeO}_3$, $\text{La}_{0.7}\text{Sr}_{0.2}\text{Co}_{0.2}\text{Fe}_{0.8}\text{O}_3$, $\text{La}_{0.7}\text{Sr}_{0.2}\text{Ni}_{0.10}\text{Co}_{0.10}\text{Fe}_{0.8}\text{O}_3$, $\text{La}_{0.7}\text{Sr}_{0.2}\text{Ni}_{0.15}\text{Co}_{0.05}\text{Fe}_{0.8}\text{O}_3$, and $\text{La}_{0.7}\text{Sr}_{0.2}\text{Ni}_{0.2}\text{Fe}_{0.8}\text{O}_3$.

2.2. Fabrication of button cell

The button cells used in this study are comprised of an YSZ electrolyte, LSM-YSZ anode and ferrite perovskite cathode. A disc of 1-inch outer diameter is punched out of a YSZ green tape procured from ESL Electroscience Laboratory, and is densified at 1450 °C. The thickness of this dense YSZ disc is 125 μm. A slurry of cathode catalyst powder is prepared by mixing with a commercial ink vehicle (NexTech materials),

which is then screen printed onto one side of the densified YSZ disc. Sintering of the screen-printed cathode layer is done at 1300 °C. The other side of the YSZ electrolyte is then screen printed with a slurry of LSM-YSZ anode and sintered at 1200 °C. For current collection from the electrodes, gold wires (ESL Electroscience) are attached onto the electrode surface using a conductive gold paste (Sigma Aldrich). The cell is then sealed onto one end of an alumina tube using a glass seal (Schott GM 31107™), the other end of which is connected to a stainless-steel compression fitting containing gas inlet-outlet. The glass seal is cured at 850 °C for half an hour inside a furnace and the temperature is then brought down to the operating temperature of 800 °C for performing electrolysis experiments. A schematic of this setup is shown in Fig. S1 of the supplementary section.

2.3. Electrochemical activity test

Different compositions of the feed gas were used for performing co-electrolysis experiments- 40%CO₂ + 3% H₂O/He, 40%CO₂ + 10% H₂O/He and 40%CO₂ + 20% H₂O/He. Total feed gas flow rate of 10 sccm was used in all these tests. Water at various concentrations was introduced into the system by flowing the gas stream through a water bubbler connected to a thermostat. A Bio-logic potentiostat SP-150 along with current booster VMP3 was used to carry out the electrochemical measurements. Prior to applying electrolysis current, flow through the cell and open circuit voltage are allowed to achieve steady state. Electrolysis is performed at three current densities: 0.7 mA/cm², 3.5 mA/cm² and 7 mA/cm². Outlet gas from the cell is sent through a water condenser and then sampled into a gas chromatograph (Shimadzu 2014) equipped with a PDHID in order to analyze the gas composition. A potentiostatic electrochemical impedance spectrum (PEIS) is collected at the end of the open circuit voltage (OCV) period. Similarly, galvanostatic electrochemical impedance spectra (GEIS) are collected under electrolysis condition.

2.4. X-ray diffraction

X-ray diffraction patterns of the calcined sample powders were collected in a Bruker D8 Advance X-ray powder diffractometer. The scans were performed in the 2θ range of 20°–60° with a step size of 0.014° and dwell time of 0.75 s. In-situ XRD was carried out in an Anton Paar HTK1200 Oven in the temperature range 30 °C–800 °C under air and He environments. These scans were also collected in 20°–60° 2θ range with 0.014° step size and 0.75 s dwell time. Miller indices of the diffraction peaks were calculated by performing a Rietveld refinement of the room temperature patterns using the General Structure Analysis System-2 (GSAS-2) software [46]. Unit cell dimensions of the samples were obtained from the in-situ XRD data using the UnitCell software [47].

2.5. Oxygen evolution under heat treatment

Heat treatment of the ferrite perovskite samples was done under a helium stream inside a 1/4-inch O.D. quartz reactor, with the outlet of the reactor connected to an MKS Cirrus bench-top residual gas analyzer. The quartz reactor was kept inside a Carbolite MTF furnace capable of heating the sample up to 1000 °C. Prior to heat treatment under helium, the sample was pretreated with 30 sccm of 10% O₂/He at 1000 °C for 1 h. Following this, the sample was cooled down to room temperature under the pretreatment environment and the flow was then switched to helium. Heating was done at a rate of 10 °C/min with a He flow rate of 30 sccm. Evolved oxygen was quantified by calibrating the mass spectrometer for oxygen using 100 μL, 500 μL and 5000 μL sample loops.

2.6. Electrical conductivity measurements

An inhouse fabricated set up (Fig. S2) was used to measure electrical conductivity of sample pellets by the four probe DC van der Pauw

method [48]. The sample pellets were prepared by first uniaxially pressing sample powder in a hydraulic press and then sintering at 1300 °C for 5 h. Density measurement of the pellets were done by an Archimedes set up prepared inhouse. Four silver wires (0.1 mm dia, 99.997% metals basis, Alfa Aesar) were connected to four points on the pellet using a conductive silver paste (Pelco™). Two of these leads were used to apply 10 mA of current by a Keithley 6220 current source, and the other two leads were used to measure the voltage drop using a Keithley 6182 sensitive nanovoltmeter. Electrical conductivity was measured by the following formula:

$$\sigma = \left(\frac{I}{V}\right)\left(\frac{l}{A}\right)$$

where I = current, V = voltage, l = distance between voltage measurement points and A = cross sectional area available for current flow.

Conductivity experiments on sample pellets were performed under a flow of 100 sccm 40% CO₂ + 3% H₂O/He at temperatures 25 °C, 200 °C, 400 °C, 500 °C, 600 °C, 700 °C and 800 °C with a half an hour stabilizing time at each temperature before performing measurements.

2.7. X-ray photoelectron spectroscopy

The nature of the surface of La_{0.7}Sr_{0.2}FeO₃, La_{0.7}Sr_{0.2}Ni_{0.2}Fe_{0.8}O₃, La_{0.7}Sr_{0.2}Ni_{0.10}Co_{0.10}Fe_{0.8}O₃, and La_{0.7}Sr_{0.2}Co_{0.2}Fe_{0.8}O₃ catalyst samples was studied using X-ray photoelectron spectra collected in a Kratos Axis Ultra XPS instrument. The X-ray was obtained from a monochromated Mg Kα source (1254 eV, 12 kV, 10 mA) and a charge neutralizer at 2.1 A, 1.3 V bias, and a charge of 2.6 V was used. Samples were loaded into an ultra-high vacuum chamber (10^{−9} torr) and spectra were collected at room temperature. Survey scans were taken in the binding energy range 1200 eV–0 eV (1 sweep, dwell time 100 ms) with a 20 eV pass energy. High resolution spectra of Fe 2p, Co 2p, Ni 2p, La 3d, Sr 3d, O 1s and C 1s regions were collected using 7 sweeps and 450 ms dwell time. Binding energies of all the regions were calibrated using standard C 1s peak at 284.5 eV, and the data were analyzed and fitted with the CasaXPS software using a Shirley background and Lorentzian (20%)- Gaussian (80%) line shape.

2.8. Ex-situ and In-situ X-ray absorption near edge spectroscopy

XANES data were collected at sector 10-BM of the Materials Research Collaborative Access Team (MRCAT) at the Advanced Photon Source (APS, Argonne National Laboratory). Ex-situ measurements on the catalyst powders were done in transmission mode. The samples were mixed with BN in the weight ratio of 1:5, ground well, and then pressed into a sample holder containing cylindrical hole of 0.12 cm² cross sectional area. Approximately 2.4 mg, 3.0 mg and 3.7 mg of the samples were mixed with BN to obtain one adsorption length at X-ray energies of 7112 eV (Fe K-edge), 7709 eV (Co K-edge) and 8333 eV (Ni K-edge), respectively. Each measurement on the sample was coupled with X-ray absorption spectra of the corresponding metal foil in order to calibrate the data for any shift in X-ray energy. In-situ XANES spectra of the cathodes were collected in fluorescence mode. A description of the experimental set-up is provided in Fig. S3. Obtained data from the samples and standards were processed using the Athena software [49].

2.9. Raman spectroscopy

Raman spectra were collected in a Horiba LabRAM HR-800 Raman Spectrometer equipped with an asymmetric Czerny Turner spectrometer (1200 g/mm grating) and CCD detector (1024 × 256 pixels, each pixel being 26 μm × 26 μm). A 100X objective was used to focus a 5 mW argon ion laser beam (514.5 nm) onto the sample and collect the backscattered photons. Only the Stokes shifted photons were sent to the detector with the help of a long wave pass edge filter. Spectra were collected with an exposure time of 50 s and averaged over 5 scans.

2.10. Diffuse reflectance infrared Fourier transform spectroscopy

A Thermoelectron Nicolet 6700 FTIR instrument containing an MCT detector was used to study high temperature co-adsorption and subsequent desorption of CO₂ and H₂O on partially reduced La_{0.7}Sr_{0.2}Ni_{0.2}Fe_{0.8}O₃ and La_{0.7}Sr_{0.2}Co_{0.2}Fe_{0.8}O₃ samples. For these experiments, the sample powders were first diluted by mixing and grinding with KBr in a weight ratio of 1:20. This diluted sample was then loaded inside a Praying Mantis DRIFTS cell capable of heating the sample up to 450 °C under the desired gaseous environment. The samples were first pretreated at 450 °C under 30 sccm He for 30 min, and background scans were taken. 30 sccm of 40% CO₂ + 3% H₂O/He was passed over the catalyst at 450 °C for 1 h and then the chamber was flushed with He for 10 min before collecting spectra to avoid interference from gas phase species. DRIFTS spectra of the catalyst surface were then collected at 450 °C under helium at different time intervals.

2.11. Temperature-programmed oxidation (TPO) to investigate coke formation

TPO on cells containing La_{0.7}Sr_{0.2}Ni_{0.2}Fe_{0.8}O₃ and La_{0.7}Sr_{0.2}Co_{0.2}Fe_{0.8}O₃ cathodes were done after they were subjected to co-electrolysis current density of 3.5 mA/cm² in a 40% CO₂ + 3% H₂O/He cathode stream at 800 °C for 24 h. 30 sccm of 10% O₂/He was used for oxidizing the deposited carbon and a mass-spectrometer was used to monitor *m/z* = 44 signal.

3. Results and discussion

3.1. X-ray diffraction studies

Fig. 1 shows in-situ XRD patterns of La_{0.7}Sr_{0.2}FeO₃, La_{0.7}Sr_{0.2}Ni_{0.2}Fe_{0.8}O₃, La_{0.7}Sr_{0.2}Co_{0.2}Fe_{0.8}O₃ and La_{0.7}Sr_{0.2}Ni_{0.1}Co_{0.1}Fe_{0.8}O₃ at various temperatures in the range 30 °C–800 °C under air. Similarly, Fig. S4 in the supplementary section shows the in-situ XRD of La_{0.7}Sr_{0.2}FeO₃, La_{0.7}Sr_{0.2}Ni_{0.2}Fe_{0.8}O₃, La_{0.7}Sr_{0.2}Co_{0.2}Fe_{0.8}O₃ and La_{0.7}Sr_{0.2}Ni_{0.1}Co_{0.1}Fe_{0.8}O₃ under helium. All the samples show pure perovskite phase at all the temperatures under air. The patterns at 30 °C for all four samples could be matched to that of La_{0.8}Sr_{0.2}FeO₃ (JCPDS file no. 35-1480) which is a perovskite oxide having orthorhombic distortions. Similar structural symmetry has been reported for LaFe_{1-x}Ni_xO₃ (0 < *x* < 0.4) by Falcon et al. [50] and for LaFe_{0.5}Ni_{0.5}O₃ by Bevilacqua et al. [51].

Fig. 1(i)–(iv) show enlarged plots of the (1 1 2) diffraction lines of the samples at each temperature. It is observed that the (1 1 2) diffraction line at 30 °C for La_{0.7}Sr_{0.2}Co_{0.2}Fe_{0.8}O₃ is broader compared to other samples and has a slight splitting. Such broadening and splitting of the principal peak is characteristic of rhombohedral distortion of the perovskite lattice [51–54]. The symmetry of a perovskite crystal structure can be indicated by the Goldschmidt tolerance factor (*t*) given by the formula shown below [43]:

$$t = (r_A + r_O) / \sqrt{2(r_B + r_O)}$$

Here, *r*_A, *r*_B and *r*_O are ionic radii of A-site, B-site and oxygen ions, respectively. For a perovskite with ideal cubic symmetry, this tolerance factor is unity. A slight decrease in this value causes rotation of the BO₆ octahedra around the crystallographic axes which leads to rhombohedral distortion of the lattice [55,56]. When the tolerance factor decreases further, the BO₆ octahedra tilts around the crystallographic axes, and this results in orthorhombic structure. Using the Shannon ionic radii for La³⁺ (CN = 12, 1.36 Å), Sr²⁺ (CN = 12, 1.18 Å), Ni³⁺ (CN = 6, 0.56 Å), Co³⁺ (CN = 6, 0.545 Å), Fe³⁺ (CN = 6, 0.645 Å) and O²⁻ (1.4 Å) [57], the tolerance factors for A-site stoichiometric compositions: La_{0.8}Sr_{0.2}FeO₃, La_{0.8}Sr_{0.2}Ni_{0.2}Fe_{0.8}O₃, La_{0.8}Sr_{0.2}Co_{0.2}Fe_{0.8}O₃, and La_{0.8}Sr_{0.2}Ni_{0.1}Co_{0.1}Fe_{0.8}O₃, are calculated to be 0.941, 0.949, 0.951 and 0.950, respectively. Since, the tolerance factor for La_{0.8}Sr_{0.2}Co_{0.2}Fe_{0.8}O₃ is the highest among these perovskite samples

and closest to unity, it is possible that La_{0.7}Sr_{0.2}Co_{0.2}Fe_{0.8}O₃ has some degree of rhombohedral distortion in the lattice, and that may cause the peaks to broaden and split slightly. It is worth mentioning that presence of a single phase rhombohedral structure will manifest itself as a more pronounced splitting of the XRD peaks as reported by Bevilacqua et al. [51]. Since the peak splitting observed here is minor, the sample has a fraction of rhombohedral phase along with orthorhombic phase.

The room temperature (1 1 2) peaks were also used to calculate the crystallite size of the perovskite samples using the Scherrer equation [58,59]:

$$\beta_L = \frac{K\lambda}{L \cos(\theta)}$$

Here, β_L is the peak broadening (FWHM) in radians, θ is half of the Bragg's angle (2 θ), *K* is a dimensionless shape factor and is taken to be 0.9 here, λ is the wavelength of Cu-K α radiation (0.15406 nm) and *L* is the crystallite size. The crystallite size for La_{0.7}Sr_{0.2}FeO₃ was calculated to be 40 nm. A decrease in the crystallite size was observed after B-site doping. This value decreased to 35 nm for La_{0.7}Sr_{0.2}Ni_{0.2}Fe_{0.8}O₃, 21 nm for La_{0.7}Sr_{0.2}Co_{0.2}Fe_{0.8}O₃, and 30 nm for La_{0.7}Sr_{0.2}Ni_{0.1}Co_{0.1}Fe_{0.8}O₃.

It can also be observed from Fig. 1 that no impurity phases are formed on heating up the sample under air. The peaks, however, are shifted to lower 2- θ values, and hence larger *d*-spacing, with increasing temperature because of the thermal expansion caused by elevated temperatures. The (1 1 2) peaks of La_{0.7}Sr_{0.2}FeO₃, La_{0.7}Sr_{0.2}Ni_{0.2}Fe_{0.8}O₃, and La_{0.7}Sr_{0.2}Ni_{0.1}Co_{0.1}Fe_{0.8}O₃ split slightly as the temperature is raised from 25 °C to 200 °C, and remains this way until 400 °C. This may indicate that the structure of these samples under air environment changes from orthorhombic at room temperature to rhombohedral at 200 °C. This evolution from orthorhombic to rhombohedral can be considered to be a change from a lower to a higher symmetry because the tolerance factor for rhombohedral perovskite is higher than that of orthorhombic perovskite and is closer to unity [55,60]. At 600 °C, the division starts to decrease and at 800 °C, it becomes a single peak again. This transformation at 800 °C can be attributed to conversion of rhombohedral to an even higher symmetric phase, i.e., a cubic structure. Unlike these three samples, La_{0.7}Sr_{0.2}Co_{0.2}Fe_{0.8}O₃ has contribution from a rhombohedral phase even at 30 °C as discussed earlier and remains this way up to 400 °C above which the splitting starts to disappear, and a single peak is evolved at 800 °C indicating the formation of a cubic perovskite. Similar alteration of rhombohedral phase to cubic phase due to increase in temperature for La_{0.6}Sr_{0.4}Co_{0.2}Fe_{0.8}O₃ perovskite oxide has been reported elsewhere [52,53]. This phase transformation, however, is reversible because when the samples are cooled down to room temperature, the crystal symmetry turned back into orthorhombic again. Since the solid oxide electrolysis cells in this study are run at 800 °C, all the cathode catalysts thus possess a cubic perovskite crystal structure at the operating temperature.

Fig. 2(a) and (b) shows the orthorhombic unit cell volumes of La_{0.7}Sr_{0.2}FeO₃, La_{0.7}Sr_{0.2}Ni_{0.2}Fe_{0.8}O₃, La_{0.7}Sr_{0.2}Co_{0.2}Fe_{0.8}O₃ and La_{0.7}Sr_{0.2}Ni_{0.1}Co_{0.1}Fe_{0.8}O₃ samples as a function of temperature under air and helium flow, respectively. In-situ XRD patterns shown in Fig. 1 and S(4) are used for calculating these unit cell parameters using the UnitCell program [47], assuming an orthorhombic (P n m a) space group. The unit cell volumes increase with increase in temperature, indicating thermal expansion of the lattice. La_{0.7}Sr_{0.2}FeO₃ contains the largest unit cell at all the temperatures. La_{0.7}Sr_{0.2}Ni_{0.2}Fe_{0.8}O₃, La_{0.7}Sr_{0.2}Co_{0.2}Fe_{0.8}O₃ and La_{0.7}Sr_{0.2}Ni_{0.1}Co_{0.1}Fe_{0.8}O₃ appear to have comparable unit cell volumes, which are less than that for La_{0.7}Sr_{0.2}FeO₃. This is due to the replacement of larger Fe³⁺ ions with smaller Ni³⁺ and Co³⁺ ions.

Average linear thermal expansion co-efficient (TEC) of the catalyst samples were calculated using the lattice parameter of the samples at various temperatures. As shown in Table S1 in the supplementary section, under air environment, La_{0.7}Sr_{0.2}FeO₃ has an average linear

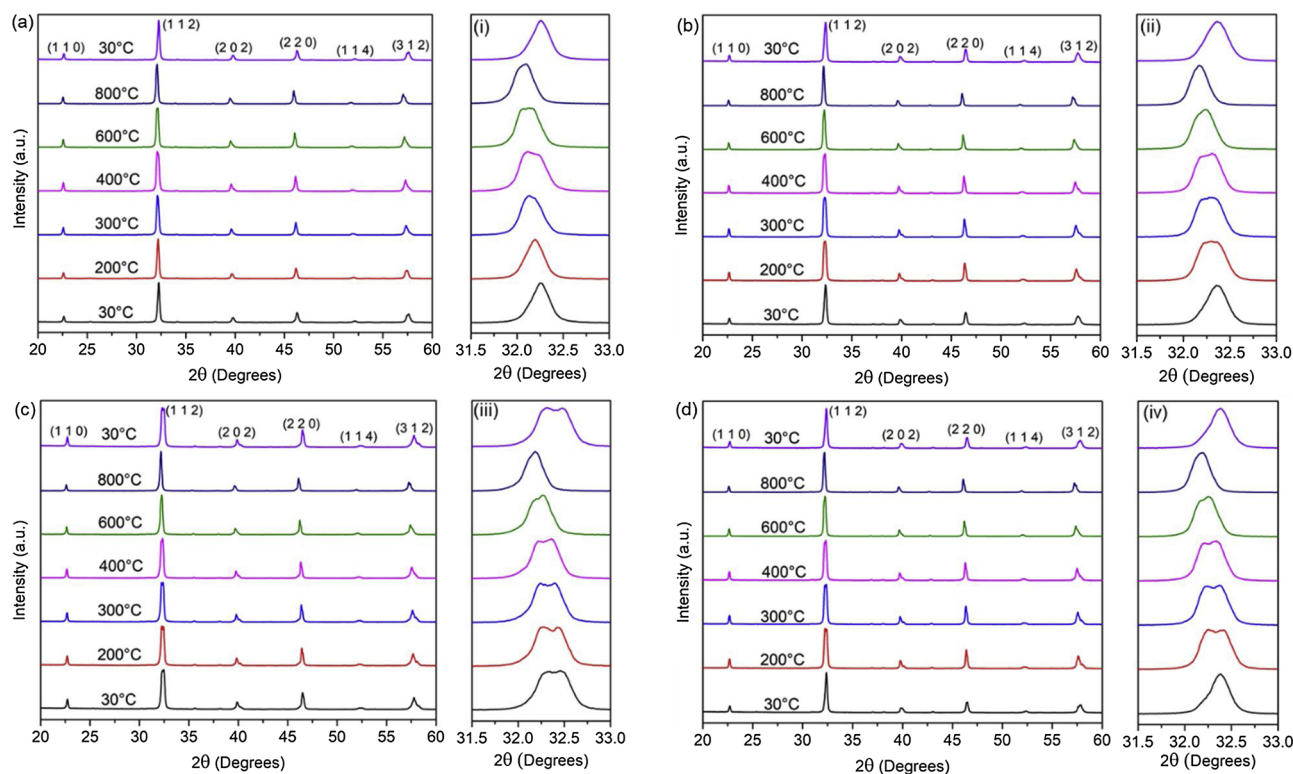


Fig. 1. In-situ X-ray diffractograms of powdered samples under air (a) $\text{La}_{0.7}\text{Sr}_{0.2}\text{FeO}_3$, (b) $\text{La}_{0.7}\text{Sr}_{0.2}\text{Ni}_{0.2}\text{Fe}_{0.8}\text{O}_3$, (c) $\text{La}_{0.7}\text{Sr}_{0.2}\text{Co}_{0.2}\text{Fe}_{0.8}\text{O}_3$, and (d) $\text{La}_{0.7}\text{Sr}_{0.2}\text{Ni}_{0.1}\text{Co}_{0.1}\text{Fe}_{0.8}\text{O}_3$ at 30 °C, 200 °C, 300 °C, 400 °C, 600 °C, 800 °C and 30 °C (after cooling). Figures (i)–(iv) show the (1 1 2) diffraction peaks in these four samples in an enlarged scale.

TEC of 10 ppm/°C, which remains the same for $\text{La}_{0.7}\text{Sr}_{0.2}\text{Co}_{0.2}\text{Fe}_{0.8}\text{O}_3$. This value, however, increases for the Ni- doped samples. Under helium, $\text{La}_{0.7}\text{Sr}_{0.2}\text{FeO}_3$ again has a TEC of 10 ppm/°C which increases after Ni and Co doping. Thus, doping with Ni and/or Co increases the TEC of the samples. TEC calculated this way is an average value for expansions caused by three different phenomena: thermal expansion of the lattice, increase in B–O bond distance due to oxygen vacancy formation, and reduction of the B-site ion relative to the amount of oxygen vacancy formed [53,61]. As shown later in section 3.3, thermally induced oxygen vacancy formation is higher in the B-site doped samples compared to the B-site undoped samples. This makes the B–O bond distance

to increase more in the doped samples with increasing temperature. As a result, the TEC of the doped samples is higher than $\text{La}_{0.7}\text{Sr}_{0.2}\text{FeO}_3$. Moreover, oxygen vacancy creation causes partial reduction of the Ni^{3+} and Co^{3+} ions into Ni^{2+} and Co^{2+} ions, respectively, so that the charge neutrality condition prevails. These bivalent ions are larger than their trivalent counterparts, and the relative increase in ionic radii is higher for Ni (0.56 Å for Ni^{3+} to 0.69 Å for Ni^{2+}) compared to Co (0.545 Å for Co^{3+} to 0.65 Å for Co^{2+}) [57]. This may be the reason that among the B-site doped samples, the Ni- doped ones have higher average TEC. In addition, as discussed in section 3.3, the Ni- doped sample creates higher oxygen vacancies than the Co- doped sample when heated up to

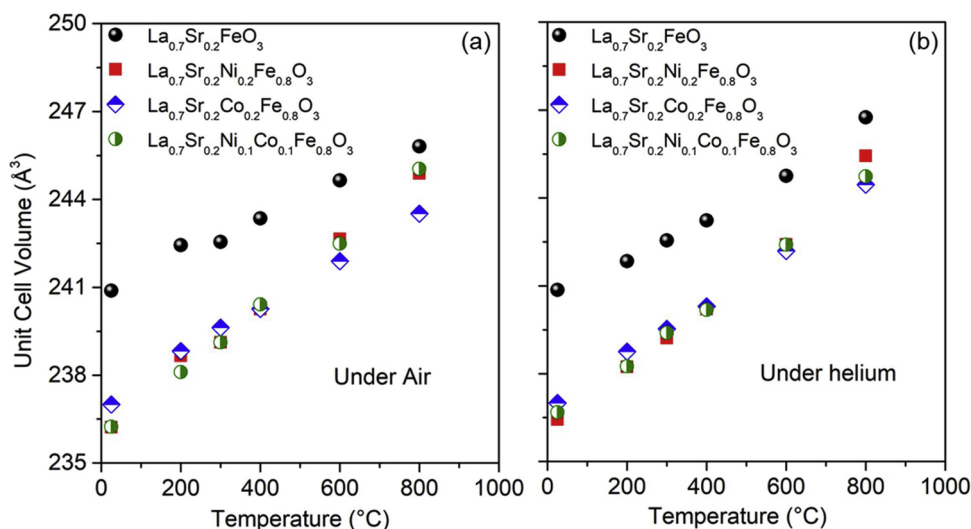


Fig. 2. Orthorhombic unit cell volumes of ferrite perovskite samples under (a) air and (b) helium environments at various temperatures obtained from the XRD patterns shown in Figs. 1 and S(4).

800 °C under helium, thus causing the lattice of the former to expand more than the latter.

3.2. Laser Raman spectroscopy

Doping of the A-site or B-site of a perovskite oxide introduces deformations not only to the cation sublattice, but also to the oxygen sublattice. However, such anion sublattice distortions do not have a strong effect on the XRD pattern because of the low scattering factor of oxygen atoms [62,63]. Raman spectroscopy is more sensitive to the vibration of oxygen ions and thus could give information about the changes occurring in the cation-anion bonds and the anion sublattice [62–65]. Raman spectra of $\text{La}_{0.7}\text{Sr}_{0.2}\text{FeO}_3$, $\text{La}_{0.7}\text{Sr}_{0.2}\text{Ni}_{0.2}\text{Fe}_{0.8}\text{O}_3$, $\text{La}_{0.7}\text{Sr}_{0.2}\text{Co}_{0.2}\text{Fe}_{0.8}\text{O}_3$ and $\text{La}_{0.7}\text{Sr}_{0.2}\text{Ni}_{0.1}\text{Co}_{0.1}\text{Fe}_{0.8}\text{O}_3$ perovskite oxide powders were collected at room temperature using a 514.5 nm argon ion laser excitation source and the results are shown in Fig. 3. The band around 150 cm^{-1} is present in all the samples and it does not show a significant change from sample to sample. This low wavenumber band can be attributed to the vibrations related to the A-site ions in the perovskite lattice [66–68]. Since the A-site ions (La and Sr) in the samples are kept constant, no appreciable change in this Raman band was observed. The bands above 200 cm^{-1} can be attributed to different modes of vibration of the B–O bonds and BO_6 octahedra [66–68]. Significant differences are observed in these high wavenumber bands among the samples. $\text{La}_{0.7}\text{Sr}_{0.2}\text{FeO}_3$ shows only one band above 200 cm^{-1} and it is positioned at 425 cm^{-1} . $\text{La}_{0.7}\text{Sr}_{0.2}\text{Co}_{0.2}\text{Fe}_{0.8}\text{O}_3$ shows two such bands at 288 cm^{-1} and 449 cm^{-1} , while $\text{La}_{0.7}\text{Sr}_{0.2}\text{Ni}_{0.2}\text{Fe}_{0.8}\text{O}_3$ shows three bands at wavenumbers 290 cm^{-1} , 423 cm^{-1} and 600 cm^{-1} . For the sample doped with both Ni and Co, i.e. $\text{La}_{0.7}\text{Sr}_{0.2}\text{Ni}_{0.1}\text{Co}_{0.1}\text{Fe}_{0.8}\text{O}_3$,

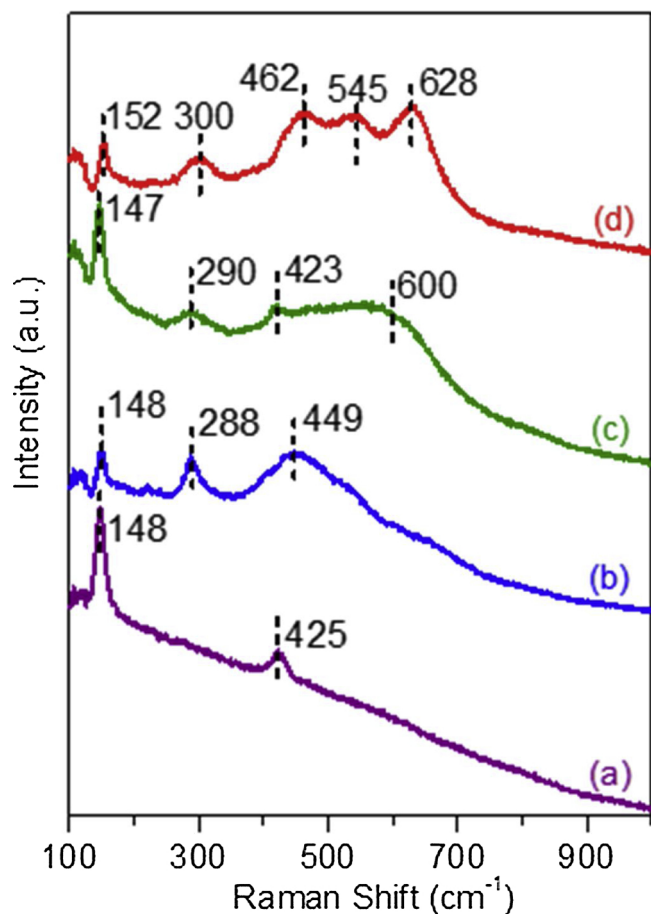


Fig. 3. Raman spectra of (a) $\text{La}_{0.7}\text{Sr}_{0.2}\text{FeO}_3$, (b) $\text{La}_{0.7}\text{Sr}_{0.2}\text{Ni}_{0.2}\text{Fe}_{0.8}\text{O}_3$, (c) $\text{La}_{0.7}\text{Sr}_{0.2}\text{Co}_{0.2}\text{Fe}_{0.8}\text{O}_3$, and (d) $\text{La}_{0.7}\text{Sr}_{0.2}\text{Ni}_{0.1}\text{Co}_{0.1}\text{Fe}_{0.8}\text{O}_3$.

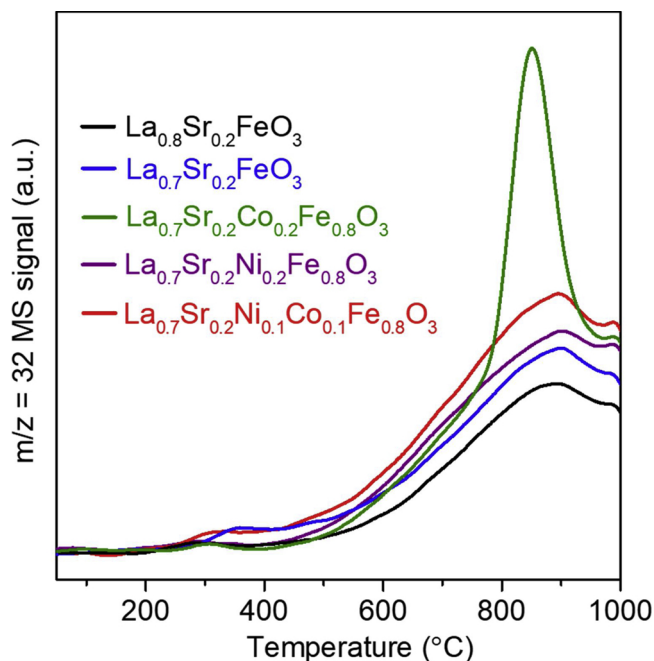


Fig. 4. Oxygen evolution from powdered ferrite perovskite catalysts during heat treatment under helium.

four bands above 200 cm^{-1} are observed: 300 cm^{-1} , 462 cm^{-1} , 545 cm^{-1} and 628 cm^{-1} . Thus, on doping the $\text{La}_{0.7}\text{Sr}_{0.2}\text{FeO}_3$ perovskite at the B-site, the BO_6 octahedral distortion changes which leads to the differences in the Raman spectra in the $> 200\text{ cm}^{-1}$ region. Such differences in the lattice deformations may cause variations in the ionic and electronic transport properties of the materials.

3.3. Oxygen evolution under heat treatment

Formation of oxygen vacancies is important in the current application because it improves the oxygen ion conductivity of the samples. Moreover, oxygen vacant sites are believed to be the active sites for adsorbing CO_2 and H_2O during electrolysis process [69]. Fig. 4 shows the oxygen ($m/z = 32$ signal) evolved as a function of temperature when 50 mg of the sample was heated under helium flow. All the samples show small oxygen peaks in the temperature range 250 °C – 350 °C . This is due to the desorption of the oxygen species adsorbed on the surface oxygen vacancies, known as α -oxygen [60,70,71]. The continuous evolution of oxygen at higher temperatures is due to the release of lattice oxygen, also known as β -oxygen [60,70,71]. Table 1 summarizes the cumulative amount of atomic oxygen evolved per mg of the sample (X) and the oxygen vacancy created per formula unit (δ) up to 800 °C , 900 °C and 1000 °C . Presence of three oxygen atoms per formula unit of the perovskite samples was assumed for calculating the theoretical amount of oxygen. $\text{La}_{0.8}\text{Sr}_{0.2}\text{FeO}_3$ yields the lowest amount of atomic oxygen. The A-site non-stoichiometric sample $\text{La}_{0.7}\text{Sr}_{0.2}\text{FeO}_3$ shows higher atomic oxygen evolution, indicating that deficiency on A-site of the perovskite helps increasing oxygen vacancies. After doping the B-site of $\text{La}_{0.7}\text{Sr}_{0.2}\text{FeO}_3$ with Ni or Co, oxygen evolution increases even further; because Ni or Co ions have lower binding energy than Fe ions do with oxygen [72–74]. For these samples, oxygen vacancy formation increases in the order: $\text{La}_{0.7}\text{Sr}_{0.2}\text{Ni}_{0.2}\text{Fe}_{0.8}\text{O}_3$, $\text{La}_{0.7}\text{Sr}_{0.2}\text{Co}_{0.2}\text{Fe}_{0.8}\text{O}_3$ and $\text{La}_{0.7}\text{Sr}_{0.2}\text{Ni}_{0.1}\text{Co}_{0.1}\text{Fe}_{0.8}\text{O}_3$ at 800 °C . Thus, at the operating temperature of 800 °C , the sample with both Ni and Co forms the highest amount of oxygen vacancy which corresponds to $\delta = 0.031$. This small fraction of oxygen vacancies created in the structure of the samples is not enough to break down the crystal, as evident from the in-situ XRD results under helium (Fig. S4). Oxygen

Table 1

Oxygen evolution from ferrite perovskites as a function of temperature. X specifies cumulative amount of oxygen atoms evolved from RT up to 800 °C, 900 °C and 1000 °C during heat treatment of ferrite perovskite materials under helium flow. δ specifies the oxygen vacancy created per formula unit during the same temperature periods.

Sample	Theoretical #moles of O atoms ($\mu\text{mol}/\text{mg}$)	X = Cumulative evolution of O atoms ($\mu\text{mol}/\text{mg}$) from RT to T δ = Oxygen vacancy formation per formula unit from RT to T					
		T = 800 °C		T = 900 °C		T = 1000 °C	
		X	δ	X	δ	X	δ
$\text{La}_{0.8}\text{Sr}_{0.2}\text{FeO}_{3-\delta}$	12.902	0.088	0.020	0.148	0.034	0.208	0.048
$\text{La}_{0.7}\text{Sr}_{0.2}\text{FeO}_{3-\delta}$	13.722	0.108	0.024	0.180	0.039	0.25	0.055
$\text{La}_{0.7}\text{Sr}_{0.2}\text{Ni}_{0.2}\text{Fe}_{0.8}\text{O}_{3-\delta}$	13.686	0.114	0.025	0.190	0.042	0.272	0.060
$\text{La}_{0.7}\text{Sr}_{0.2}\text{Co}_{0.2}\text{Fe}_{0.8}\text{O}_{3-\delta}$	13.684	0.124	0.027	0.286	0.063	0.376	0.082
$\text{La}_{0.7}\text{Sr}_{0.2}\text{Ni}_{0.1}\text{Co}_{0.1}\text{Fe}_{0.8}\text{O}_{3-\delta}$	13.686	0.142	0.031	0.236	0.052	0.328	0.072

vacancies in the samples increase with further increase in temperature up to 900 °C and 1000 °C. As seen in Fig. 4, the Co-doped catalyst $\text{La}_{0.7}\text{Sr}_{0.2}\text{Co}_{0.2}\text{Fe}_{0.8}\text{O}_3$ shows a much sharper peak at 850 °C compared to other samples which can be attributed to the reduction of Co^{3+} ions to Co^{2+} ions as reported in the literature [70,75]. Inclusion of Ni in the perovskite structure stabilizes the Co oxidation state, as shown by Longo and co-workers [76] using in-situ XANES, and that may be the reason behind the absence of such sharp reduction of Co^{3+} to Co^{2+} in $\text{La}_{0.7}\text{Sr}_{0.2}\text{Ni}_{0.1}\text{Co}_{0.1}\text{Fe}_{0.8}\text{O}_3$ at high temperature.

3.4. Electronic conductivity measurements

Strontium-doped lanthanum ferrite is a mixed ionic and electronic conductor (MIEC), and hence have both electronic and ionic conductivities, the former being an order of magnitude higher than the latter [77,78]. The total conductivity measurements performed for this study can therefore be effectively attributed to electronic conductivity. All the samples were pelletized and sintered at 1300 °C under air. The measured conductivity values depend on the sample preparation procedure and pellet sintering temperature. That is why 1300 °C is used as the sintering temperature in this study, as it is the same temperature at which the cathode catalysts are sintered over the YSZ electrolyte following screen printing. Densities of the sintered pellets were in between 5.9 g/cc–6.2 g/cc, which is 96%–100% of the theoretical density of the materials calculated using the room temperature unit cell volumes. Conductivity measurements were performed under a 40% CO_2 + 3% $\text{H}_2\text{O}/\text{He}$ mixed gas environment. The same composition of gas is used as a feed for the co-electrolysis experiments discussed later.

Fig. 5(a) shows the conductivities of doped ferrite catalysts in the temperature range 298 K–1073 K. In general, the B-site undoped $\text{La}_{0.7}\text{Sr}_{0.2}\text{FeO}_3$ shows the lowest conductivity, whereas the Ni-doped $\text{La}_{0.7}\text{Sr}_{0.2}\text{Ni}_{0.2}\text{Fe}_{0.8}\text{O}_3$ has the highest electronic conductivity. $\text{La}_{0.7}\text{Sr}_{0.2}\text{Co}_{0.2}\text{Fe}_{0.8}\text{O}_3$ has a higher electronic conductivity than $\text{La}_{0.7}\text{Sr}_{0.2}\text{FeO}_3$, but lower than both $\text{La}_{0.7}\text{Sr}_{0.2}\text{Ni}_{0.2}\text{Fe}_{0.8}\text{O}_3$ and $\text{La}_{0.7}\text{Sr}_{0.2}\text{Ni}_{0.1}\text{Co}_{0.1}\text{Fe}_{0.8}\text{O}_3$. At 800 °C, which is the operating temperature of SOECs in this study, conductivities of $\text{La}_{0.7}\text{Sr}_{0.2}\text{FeO}_3$, $\text{La}_{0.7}\text{Sr}_{0.2}\text{Co}_{0.2}\text{Fe}_{0.8}\text{O}_3$, $\text{La}_{0.7}\text{Sr}_{0.2}\text{Ni}_{0.2}\text{Fe}_{0.8}\text{O}_3$, and $\text{La}_{0.7}\text{Sr}_{0.2}\text{Ni}_{0.1}\text{Co}_{0.1}\text{Fe}_{0.8}\text{O}_3$ are 80 $\text{S}\cdot\text{cm}^{-1}$, 141 $\text{S}\cdot\text{cm}^{-1}$, 159 $\text{S}\cdot\text{cm}^{-1}$, and 163 $\text{S}\cdot\text{cm}^{-1}$, respectively. These values are comparable to the electronic conductivity values for doped LSF-type perovskites under air environment reported in the literature [79,80]. Conductivities of all the samples increase with an increase in temperature, reaches a maximum and then drops with at higher temperatures. The samples $\text{La}_{0.7}\text{Sr}_{0.2}\text{FeO}_3$, $\text{La}_{0.7}\text{Sr}_{0.2}\text{Ni}_{0.2}\text{Fe}_{0.8}\text{O}_3$ and $\text{La}_{0.7}\text{Sr}_{0.2}\text{Ni}_{0.1}\text{Co}_{0.1}\text{Fe}_{0.8}\text{O}_3$ reach their maximum conductivity values at 873 K, while $\text{La}_{0.7}\text{Sr}_{0.2}\text{Co}_{0.2}\text{Fe}_{0.8}\text{O}_3$ appears to reach its maximum conductivity at 973 K. A decrease in the electronic conductivity of these samples at higher temperatures takes place due to the formation of oxygen vacancies. The oxygen vacancy formation process due to heating of a $\text{La}_{0.8}\text{Sr}_{0.2}\text{BO}_3$ ($\text{B} = \text{Fe}, \text{Ni}, \text{Co}$) perovskite oxide can be denoted by the Kröger-Vink notation as follows:

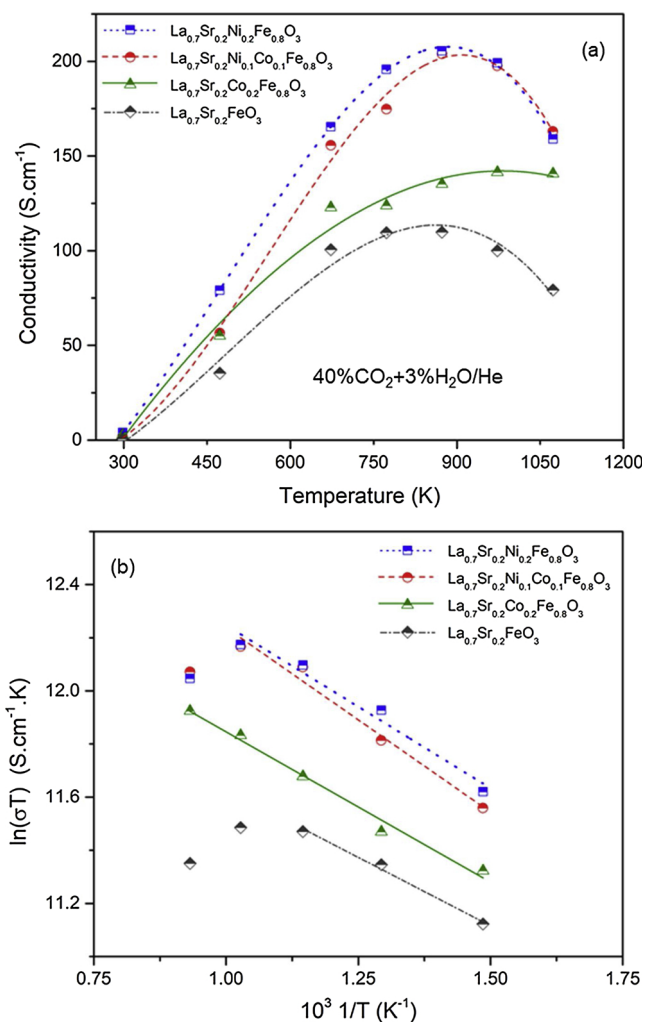
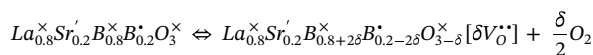


Fig. 5. (a) Electronic conductivity of ferrite perovskite pellets under 40% CO_2 + 3% $\text{H}_2\text{O}/\text{He}$ environment in the temperature range of 300–800 °C. (b) Arrhenius plot of the electrical conductivity values shown in Fig. 5(a).



In this equation, ‘x’ denotes neutral effective charge, ‘•’ denotes a negative effective charge, ‘••’ denotes a positive effective charge, $V_O^{\bullet\bullet}$ is an oxygen vacancy having two effective positive charges and B^{\bullet} is a p-type charge carrier containing one positive effective charge. As this equation shows, for every oxygen vacancy created, two p-type charge carriers are eliminated. In other words, two B^{4+} ions are converted to B^{3+} ions for

each oxygen vacancy created. Thus, at higher temperatures, the charge carrier concentration in the sample decreases.

Doped lanthanum strontium ferrites have been shown to exhibit p-type conduction following a small polaron conduction mechanism [51,80,81]. Charge carriers for such materials is a p-type carrier possessing an effective positive charge, e.g., $\text{Fe}^{4+}/\text{Fe}^{3+}$, $\text{Co}^{4+}/\text{Co}^{3+}$, $\text{Ni}^{4+}/\text{Ni}^{3+}$ redox couples. This type of conduction can be described by the following Arrhenius-type equation:

$$\sigma = \frac{A}{T} \exp\left(-\frac{E_a}{kT}\right)$$

Here, σ is electrical conductivity, A is a pre-exponential factor which depends on the material property and charge carrier density, E_a is activation energy for the hopping of polarons, k is the Boltzmann constant and T is the absolute temperature. When the natural logarithm of σT is plotted against $1/T$, a straight line is obtained with the slope numerically equal to E_a/k . The conductivity data obtained under 40% CO_2 + 3% $\text{H}_2\text{O}/\text{He}$ in the temperature range 673 K–1073 K are plotted in this form in Fig. 5(b). It can be observed that not all the samples follow small polaron conduction mechanism in this entire temperature range. $\text{La}_{0.7}\text{Sr}_{0.2}\text{Co}_{0.2}\text{Fe}_{0.8}\text{O}_3$ follows this mechanism in the whole range 673–1073 K, whereas both $\text{La}_{0.7}\text{Sr}_{0.2}\text{Ni}_{0.1}\text{Co}_{0.1}\text{Fe}_{0.8}\text{O}_3$ and $\text{La}_{0.7}\text{Sr}_{0.2}\text{Ni}_{0.2}\text{Fe}_{0.8}\text{O}_3$ follow in 673 K–973 K, and $\text{La}_{0.7}\text{Sr}_{0.2}\text{FeO}_3$ follows only in the range 673 K–873 K. The activation energy obtained from these plots in these temperature ranges are shown in Table S2. These values are similar to the activation energies reported in the literature for $\text{La}_{0.8}\text{Sr}_{0.2}\text{Co}_{0.2}\text{Fe}_{0.8}\text{O}_3$ (0.14 eV) under air environment [80].

3.5. X-ray photoelectron spectroscopy (XPS)

XPS measurements were done to identify the oxidation states of the metal ions as well as the atomic concentrations on the surface of the samples. Fig. 6(a) shows the O 1s region of the photoelectron spectra of $\text{La}_{0.7}\text{Sr}_{0.2}\text{FeO}_3$, $\text{La}_{0.7}\text{Sr}_{0.2}\text{Co}_{0.2}\text{Fe}_{0.8}\text{O}_3$, $\text{La}_{0.7}\text{Sr}_{0.2}\text{Ni}_{0.2}\text{Fe}_{0.8}\text{O}_3$, and $\text{La}_{0.7}\text{Sr}_{0.2}\text{Ni}_{0.1}\text{Co}_{0.1}\text{Fe}_{0.8}\text{O}_3$. All the spectra contain two types of oxygen species: lattice oxygen (528.2 eV) and surface adsorbed oxygen (530.7 eV) [52,60,82–85]. Once the relative concentrations of the lattice oxygen (O^{2-}) and adsorbed oxygen (O_{ads}) species are known from deconvolution, the absolute concentrations of these species on the surface can be calculated by using the survey scan. Table 3 shows the

atomic concentrations on the surface of the samples, including those of O_{ads} and O^{2-} . The concentration of O_{ads} increases upon B-site doping with Ni or Co or both. Thus B-site doping leads to creation of more oxygen vacant sites on the surface, as well as in the bulk as discussed earlier, which can assist in the activation of CO_2 and H_2O molecules during electrolysis.

Fig. 6(b) shows Fe 2p region of the photoelectron spectra along with the deconvoluted components. All the samples needed similar peak models to fit their spectra. The components at around 710.4 eV and 724 eV binding energies in all the samples belong to Fe^{3+} species, whereas the components at approximately 713.8 eV and 727.4 eV belong to Fe^{4+} species [60,86]. The presence of a shake-up satellite peak at 719.5 eV (~9 eV higher than the Fe^{3+} component of Fe 2p_{3/2} peak) confirms that the component at 710.4 eV is indeed due to a Fe^{3+} species. Thus, the catalyst samples under investigation contains both Fe^{3+} and Fe^{4+} on the surface. Similar observations have also been reported by other studies for lanthanum strontium ferrite-type perovskites [60,86]. Presence of $\text{Fe}^{4+}/\text{Fe}^{3+}$ redox couples is important in these materials as they work as p-type charge carriers, and thus providing electronic conductivity to the catalysts. Higher the $\text{Fe}^{4+}/\text{Fe}^{3+}$ ratio, higher will be the charge carrier concentration, and hence higher should be the electronic conductivity. Table 2 lists the relative amounts of Fe^{4+} and Fe^{3+} in $\text{La}_{0.7}\text{Sr}_{0.2}\text{FeO}_3$, $\text{La}_{0.7}\text{Sr}_{0.2}\text{Co}_{0.2}\text{Fe}_{0.8}\text{O}_3$, $\text{La}_{0.7}\text{Sr}_{0.2}\text{Ni}_{0.2}\text{Fe}_{0.8}\text{O}_3$, and $\text{La}_{0.7}\text{Sr}_{0.2}\text{Ni}_{0.1}\text{Co}_{0.1}\text{Fe}_{0.8}\text{O}_3$. It is observed that after doping the B-site with Ni and/or Co, the concentration of Fe^{4+} increases, and this improves the conductivity of the materials. However, it is not possible to draw a one-to-one relationship between the electronic conductivity of the catalyst samples and the obtained $\text{Fe}^{4+}/\text{Fe}^{3+}$ ratios because of two reasons: (a) the $\text{Fe}^{4+}/\text{Fe}^{3+}$ ratio obtained from XPS is only a surface property, whereas conductivity is a bulk property; (b) even though $\text{Fe}^{4+}/\text{Fe}^{3+}$ couples are the majority charge carrier in these samples, the Ni and Co-doped samples also contain $\text{Ni}^{4+}/\text{Ni}^{3+}$ and $\text{Co}^{4+}/\text{Co}^{3+}$ redox couples, which may work as charge carriers in these samples. In section 3.6, using XANES data we show that all of these three redox couples are also present in the bulk of these samples.

Fig. 6(c) shows the Co 2p regions of $\text{La}_{0.7}\text{Sr}_{0.2}\text{Co}_{0.2}\text{Fe}_{0.8}\text{O}_3$ and $\text{La}_{0.7}\text{Sr}_{0.2}\text{Ni}_{0.1}\text{Co}_{0.1}\text{Fe}_{0.8}\text{O}_3$. The appearance of the satellite peaks at the binding energies 786.7 eV and 801.6 eV indicates the presence of Co^{2+} on the surfaces of both samples [87–89]. The 2p_{3/2} and 2p_{1/2}

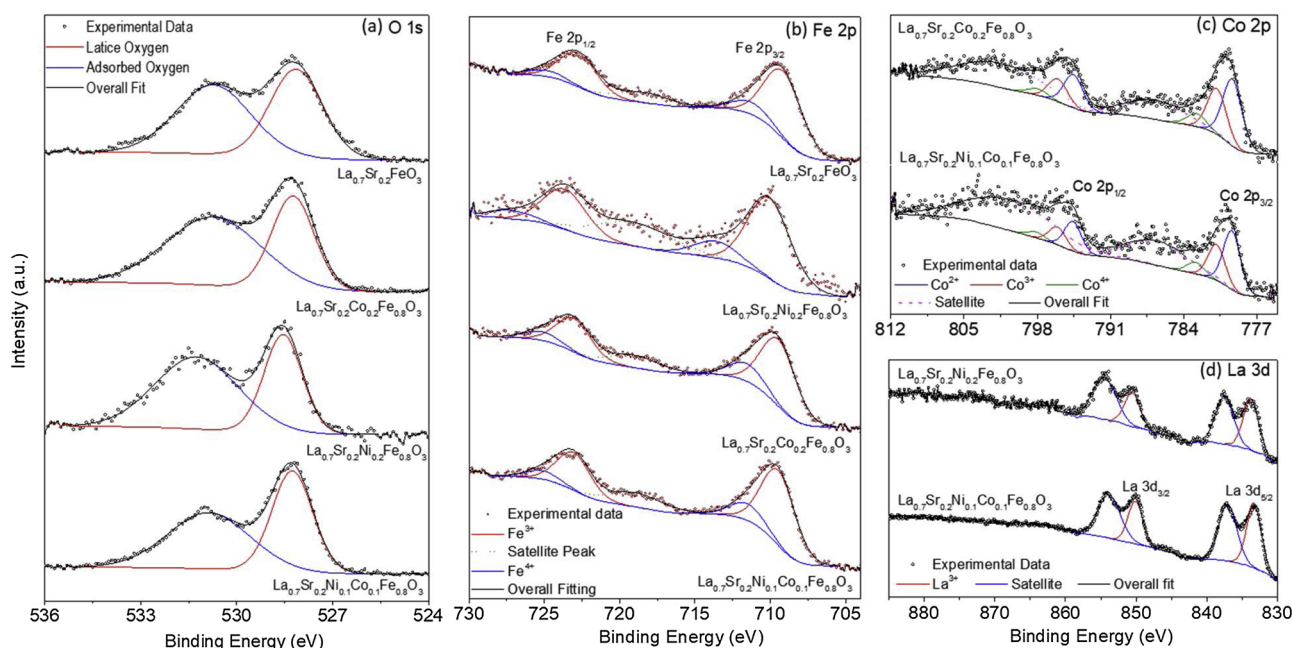


Fig. 6. X-ray photoelectron spectra of ferrite perovskite oxides: (a) O 1s region, (b) Fe 2p region, (c) Co 2p region, (d) La 3d region.

Table 2

Relative distribution of the oxidation states of Fe and Co on the surface of ferrite perovskite catalysts.

Sample	Oxidation state of Fe (percentage)		Oxidation state of Co (percentage)		
	Fe ³⁺	Fe ⁴⁺	Co ²⁺	Co ³⁺	Co ⁴⁺
La _{0.7} Sr _{0.2} FeO ₃	84.7	15.3	–	–	–
La _{0.7} Sr _{0.2} Ni _{0.1} Co _{0.1} Fe _{0.8} O ₃	78.7	21.3	–	–	–
La _{0.7} Sr _{0.2} Co _{0.2} Fe _{0.8} O ₃	82.6	17.4	59.5	29.7	10.8
La _{0.7} Sr _{0.2} Ni _{0.1} Co _{0.1} Fe _{0.8} O ₃	81.3	18.7	53.1	36.5	10.4

components of the Co²⁺ species can be seen at 779.3 eV and 794.5 eV, respectively. Similarly, the ones at 780.8 eV and 796.0 eV can be assigned to Co³⁺, whereas the ones at 782.7 eV and 797.9 eV can be assigned to Co⁴⁺ [88,90]. Thus, La_{0.7}Sr_{0.2}Co_{0.2}Fe_{0.8}O₃ and La_{0.7}Sr_{0.2}Ni_{0.1}Co_{0.1}Fe_{0.8}O₃ contains cobalt in three oxidation states: Co²⁺, Co³⁺ and Co⁴⁺. Table 2 shows the relative concentrations of these three Co oxidation states.

La 3d regions of La_{0.7}Sr_{0.2}Ni_{0.2}Fe_{0.8}O₃ and La_{0.7}Sr_{0.2}Ni_{0.1}Co_{0.1}Fe_{0.8}O₃ are shown in Fig. 6(d). The binding energies of the 3d_{5/2} peak and the 3d_{3/2} peak in these two samples are quite similar. Deconvolution shows that the binding energy of the 3d_{5/2} peak is approximately 833.5 eV and that of 3d_{3/2} is 850.3 eV. These binding energies can be assigned to a La³⁺ species [48,91–94]. This trivalent oxidation state of La ions can also be confirmed by the presence of satellite peaks at 837.3 eV and 854.2 eV, which are approximately at 4 eV higher binding energies than 3d_{5/2} and 3d_{3/2} core-line peaks [93,94]. The appearance of such satellite peaks is dependent on the coordination environment of La atoms and is believed to arise from ligand-to-metal charge transfer shake-up process. Similar La 3d spectra have been obtained for the samples La_{0.7}Sr_{0.2}FeO₃ and La_{0.7}Sr_{0.2}Co_{0.2}Fe_{0.8}O₃ (not shown here). Strontium is mainly present as Sr²⁺ on the surface of these catalysts along with surface carbonates and strontium suboxide (SrO) (not shown here).

Fig. 6(d) also shows an extended binding energy range of 860 eV–885 eV. Ni 2p photoelectron spectra should appear in the binding energy range 850 eV–885 eV [95]. However, no such peaks can be seen in this figure, indicating that nickel atoms are not present on the surface of the Ni-doped catalyst samples. In other words, Ni preferentially stays in the bulk of the structure rather than the surface of these A-site deficient ferrite perovskites. Interestingly, even though the atomic percentages of Co used for doping is similar to that of Ni, Co 2p spectra shows the presence of Co on the surface.

3.6. Ex-situ X-ray absorption near edge structure (XANES)

Fig. S5(a) of the Supplementary Information section compares the Fe K-edge XANES spectra for the ferrite catalyst samples to that of Fe-foil, FeO and Fe₂O₃ standards. When the edge energies of La_{0.7}Sr_{0.2}FeO₃, La_{0.7}Sr_{0.2}Co_{0.2}Fe_{0.8}O₃, La_{0.7}Sr_{0.2}Ni_{0.2}Fe_{0.8}O₃, and La_{0.7}Sr_{0.2}Ni_{0.1}Co_{0.1}Fe_{0.8}O₃ are compared to those of the standards, their positions are found to be on the higher energy side. Thus, the oxidation state of iron in these samples is higher than +3. In other words, these ferrite perovskite materials contain Fe⁴⁺/Fe³⁺ redox couples in the

bulk as well. These redox couples act as p-type charge carriers as mentioned in section 3.4.

Fig. S5(b) shows Co K-edge XANES of La_{0.7}Sr_{0.2}Co_{0.2}Fe_{0.8}O₃ and La_{0.7}Sr_{0.2}Ni_{0.1}Co_{0.1}Fe_{0.8}O₃ along with the standards Co-foil, CoO and Co₂O₃. Edge energy positions of the samples are found to be higher than that of Co₂O₃, indicating that oxidation state of Co is more than +3 in both these Co-doped ferrite perovskite samples. Thus, Co⁴⁺/Co³⁺ redox couples that can act as p-type charge carriers are present in the bulk these samples. Fig. S5(c) compares the Ni K-edge XANES of the Ni-doped ferrite samples to those of the standards: Ni-foil, NiO and Ni₂O₃, which shows that Ni is also present in an oxidation state of higher than +3.

Combining XPS and XANES data, it can be said that the samples La_{0.7}Sr_{0.2}FeO₃, La_{0.7}Sr_{0.2}Co_{0.2}Fe_{0.8}O₃, La_{0.7}Sr_{0.2}Ni_{0.2}Fe_{0.8}O₃, and La_{0.7}Sr_{0.2}Ni_{0.1}Co_{0.1}Fe_{0.8}O₃ contain Fe⁴⁺/Fe³⁺, Co⁴⁺/Co³⁺ and Ni⁴⁺/Ni³⁺ redox couples both on the surface and in the bulk.

3.7. Electrochemical activity for CO₂+H₂O co-electrolysis

Co-electrolysis of CO₂+H₂O was performed on a 10 sccm cathode feed stream having 40% CO₂, 3% H₂O and the balance helium. Flux of H₂ and CO obtained during this process are shown in Fig. 7(a) and (b), respectively. Five compositions of ferrite cathode materials were tested for their electrochemical activity: La_{0.7}Sr_{0.2}FeO₃, La_{0.7}Sr_{0.2}Co_{0.2}Fe_{0.8}O₃, La_{0.7}Sr_{0.2}Ni_{0.1}Co_{0.1}Fe_{0.8}O₃, La_{0.7}Sr_{0.2}Ni_{0.15}Co_{0.05}Fe_{0.8}O₃, and La_{0.7}Sr_{0.2}Ni_{0.2}Fe_{0.8}O₃. The absolute values of electrolysis current densities (i.e. without a negative sign) is used in this discussion. For each current density, flux of H₂ is the lowest for La_{0.7}Sr_{0.2}FeO₃ and the highest for La_{0.7}Sr_{0.2}Ni_{0.2}Fe_{0.8}O₃. Among the other three cathodes, production of H₂ increases with increase in Ni content in the material. Thus, presence of Ni in the cathode material enhances production of H₂ during co-electrolysis. Flux of CO during co-electrolysis, as seen in Fig. 7(b), decreases for La_{0.7}Sr_{0.2}Co_{0.2}Fe_{0.8}O₃ when compared to B-site undoped sample, La_{0.7}Sr_{0.2}FeO₃. This was not the case for H₂ production where the undoped cathode produced the lowest H₂. The Ni and Co-doped samples La_{0.7}Sr_{0.2}Ni_{0.1}Co_{0.1}Fe_{0.8}O₃ and La_{0.7}Sr_{0.2}Ni_{0.15}Co_{0.05}Fe_{0.8}O₃ produce CO at a higher rate than La_{0.7}Sr_{0.2}Co_{0.2}Fe_{0.8}O₃; however, it is still lower than the B-site undoped sample. Production rate of CO is found to be lowest for the cell containing La_{0.7}Sr_{0.2}Ni_{0.2}Fe_{0.8}O₃ cathode. The electrochemical activity tests thus suggest that doping the ferrite perovskite cathodes with Ni improves the production of H₂ while it affects the production of CO in a negative manner.

Fig. 7(c) shows the total Faradaic efficiencies (total production of syngas) obtained from the ferrite cathodes during co-electrolysis processes. It is seen that La_{0.7}Sr_{0.2}FeO₃ cathode has a moderate Faradaic efficiency (~75% - 85%) for the current densities used in this study, and it is the lowest for La_{0.7}Sr_{0.2}Co_{0.2}Fe_{0.8}O₃ (~45% - 65%). This decrease in Faradaic efficiency for the cobalt-doped sample when compared to undoped sample is mainly due to the significant decrease in CO production rate during co-electrolysis. As shown later, this cathode electrolyzes CO₂ all the way to carbon, thus reducing the yield of CO as well as the related Faradaic efficiency. The Faradaic efficiencies of the Ni-containing samples are high (~100%) irrespective of the amount of Ni in the material. It is noteworthy that high efficiencies are observed for the

Table 3

Surface atomic composition of the ferrite perovskite samples obtained from XPS data. O_{ads} is adsorbed oxygen, O²⁻ is lattice oxygen.

Samples	Percentage surface atomic composition			O ²⁻ (Lattice Oxygen)	O _{ads}
	A-site (La + Sr)	B-site (Ni + Co + Fe)	O		
La _{0.7} Sr _{0.2} FeO ₃	18.48	9.87	71.65	34.12	37.53
La _{0.7} Sr _{0.2} Ni _{0.2} Fe _{0.8} O ₃	19.44	7.28	73.27	28.18	45.09
La _{0.7} Sr _{0.2} Co _{0.2} Fe _{0.8} O ₃	17.84	9.15	73.02	28.09	44.93
La _{0.7} Sr _{0.2} Ni _{0.1} Co _{0.1} Fe _{0.8} O ₃	18.95	8.36	72.68	33.40	39.30

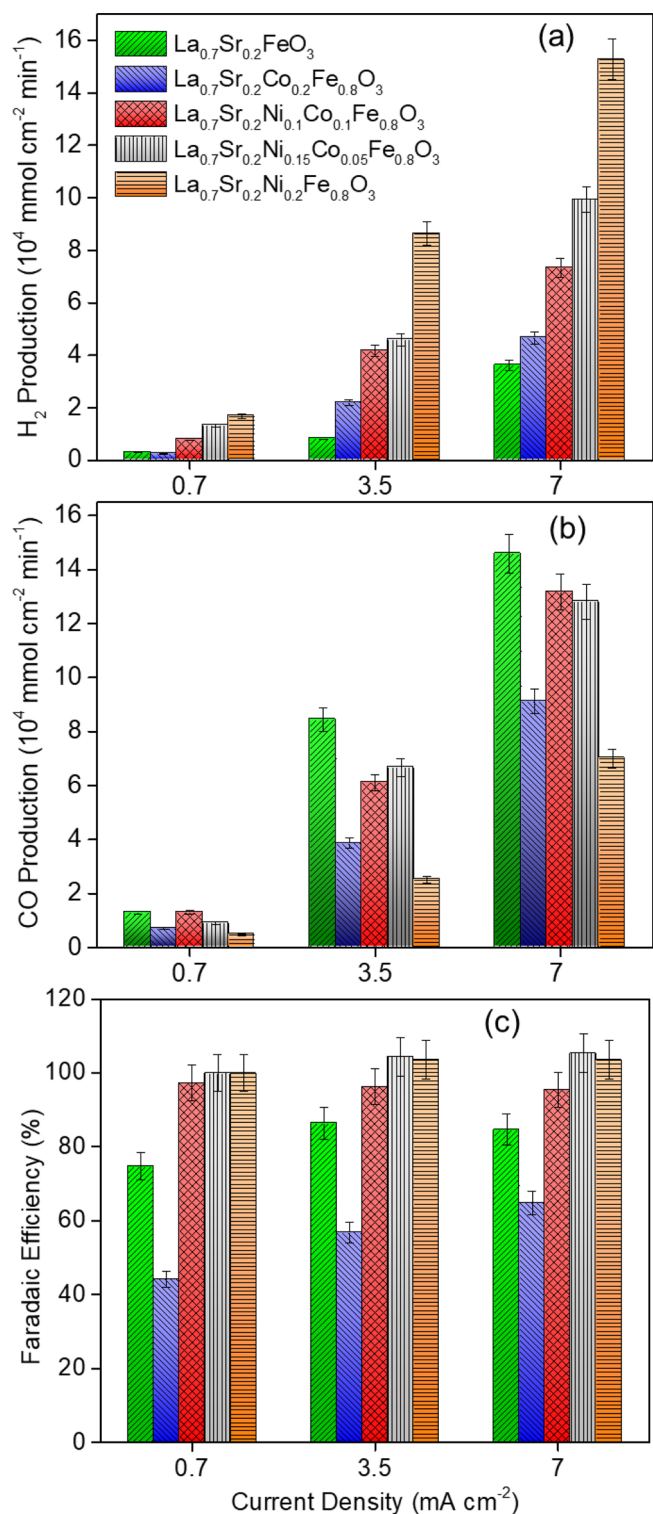


Fig. 7. Production rate of (a) H_2 and (b) CO normalized over electrode geometric surface area during co-electrolysis of 40% CO_2 + 3% H_2O /He at 800 °C over ferrite perovskite cathodes at three different electrolysis current densities, (c) Total Faradaic efficiency of the co-electrolysis process.

Ni-containing cathodes despite the lower CO production rates they exhibit, because higher H_2 production rates are observed with these cathodes, thus maintaining a high total syngas (H_2 + CO) production rate. Hence, it can be said that different cathodes used in this study will produce syngas with different H_2/CO ratios.

Table 4

H_2/CO ratio of the syngas produced from high temperature co-electrolysis of 40% CO_2 + 3% H_2O /He over ferrite perovskite cathodes at 800 °C.

Sample	0.7 mA cm^{-2}	3.5 mA cm^{-2}	7 mA cm^{-2}
$\text{La}_{0.7}\text{Sr}_{0.2}\text{FeO}_3$	0.23	0.13	0.25
$\text{La}_{0.7}\text{Sr}_{0.2}\text{Co}_{0.2}\text{Fe}_{0.8}\text{O}_3$	0.35	0.57	0.52
$\text{La}_{0.7}\text{Sr}_{0.2}\text{Ni}_{0.1}\text{Co}_{0.1}\text{Fe}_{0.8}\text{O}_3$	0.61	0.68	0.56
$\text{La}_{0.7}\text{Sr}_{0.2}\text{Ni}_{0.15}\text{Co}_{0.05}\text{Fe}_{0.8}\text{O}_3$	1.47	0.69	0.80
$\text{La}_{0.7}\text{Sr}_{0.2}\text{Ni}_{0.2}\text{Fe}_{0.8}\text{O}_3$	3.54	3.42	2.18

The ratio of H_2 to CO in the produced syngas determines its usability as a feedstock in the industry. High-temperature co-electrolysis allows production of syngas with a control over the H_2/CO ratio. Wang and co-workers [96] showed that syngas with H_2/CO of 2:1 can be produced over $\text{Sr}_{1.5}\text{Fe}_{1.5}\text{Mo}_{0.5}\text{O}_6$ cathode by co-electrolyzing CO_2 and H_2O . Similarly, Maide and co-workers [20] used a $\text{La}_{0.8}\text{Sr}_{0.2}\text{Cr}_{0.5}\text{Mn}_{0.5}\text{O}_3$ cathode for co-electrolysis and showed that H_2/CO in the produced syngas is a function of temperature and the electrode microstructure. In the present study, it was found that the composition of syngas depends on many parameters, including current, cell voltage, feed gas composition and electrode material composition. Table 4 shows the H_2/CO ratios obtained for the ferrite perovskite cathodes during co-electrolysis process at different current densities. For each current, H_2/CO ratio is the lowest for the syngas produced by $\text{La}_{0.7}\text{Sr}_{0.2}\text{FeO}_3$ cathode. This ratio marginally increases after doping the cathode material with cobalt. H_2/CO ratio increases even further for the Ni-doped samples. In fact, H_2/CO ratio increases with increase in Ni content in the samples. At 7 mA/cm^2 current density, a H_2/CO ratio of 2:1 from $\text{La}_{0.7}\text{Sr}_{0.2}\text{Ni}_{0.2}\text{Fe}_{0.8}\text{O}_3$ cathode, 1:1 from $\text{La}_{0.7}\text{Sr}_{0.2}\text{Ni}_{0.15}\text{Co}_{0.05}\text{Fe}_{0.8}\text{O}_3$ cathode and 1:2 from $\text{La}_{0.7}\text{Sr}_{0.2}\text{Ni}_{0.1}\text{Co}_{0.1}\text{Fe}_{0.8}\text{O}_3$ is obtained in the produced syngas. Thus, presence of Ni in the cathode material helps not only improving the Faradic efficiency of the electrolysis process, but also producing a H_2 rich syngas. Since, composition of syngas is an important factor when it is used as a raw material for producing chemicals, being able to control the H_2/CO ratio by changing the composition of the cathode adds to the advantages of an SOEC. Moreover, the H_2/CO ratio decreases with increasing electrolysis current for all the cathode materials. This implies that voltage dependence of CO_2 and H_2O electrolysis kinetics are different [18] on these cathode materials. In section 3.12, it is shown that H_2/CO ratio also changes with change in $\text{H}_2\text{O}/\text{CO}_2$ ratio in the feed. Thus, the syngas composition can also be tuned by varying the different operating conditions of the electrolysis cells.

3.8. In-situ XANES of cathodes under co-electrolysis conditions

Fig. S6(a), (b) and (c) shows the in-situ Fe K-edge XANES of $\text{La}_{0.7}\text{Sr}_{0.2}\text{FeO}_3$, $\text{La}_{0.7}\text{Sr}_{0.2}\text{Ni}_{0.2}\text{Fe}_{0.8}\text{O}_3$, and $\text{La}_{0.7}\text{Sr}_{0.2}\text{Co}_{0.2}\text{Fe}_{0.8}\text{O}_3$ cathodes, respectively, under OCV at room temperature and 800 °C, as well as under an applied current density of 6 mA/cm^2 at 800 °C in a co-electrolysis environment consisting of 40% CO_2 and 3% H_2O in helium balance. The edge positions of the spectra for all three catalysts are also shown in the tables inside the figures. The changes in edge positions in the XANES could be due to a change in oxidation state of the element or a change in its co-ordination environment. It can be observed from the XANES data and the tables that the edge positions do not change appreciably when the experimental conditions are varied. A slight variation observed in the range 0 eV–0.4 eV which is within the experimental error (the spectral resolution for Fe K-edge XANES in this beamline is 0.36 eV). Thus, it can be inferred that there is no appreciable change in the oxidation state or co-ordination of Fe in the cathode material when the solid oxide electrolysis cell is heated under OCV condition from room temperature to 800 °C in CO_2 + H_2O gas environment as well as during the application of electrolysis current at 800 °C.

Fig. 8(a) shows the Ni K-edge XANES of $\text{La}_{0.7}\text{Sr}_{0.2}\text{Ni}_{0.2}\text{Fe}_{0.8}\text{O}_3$ cathode under OCV at room temperature, under OCV at 800 °C and

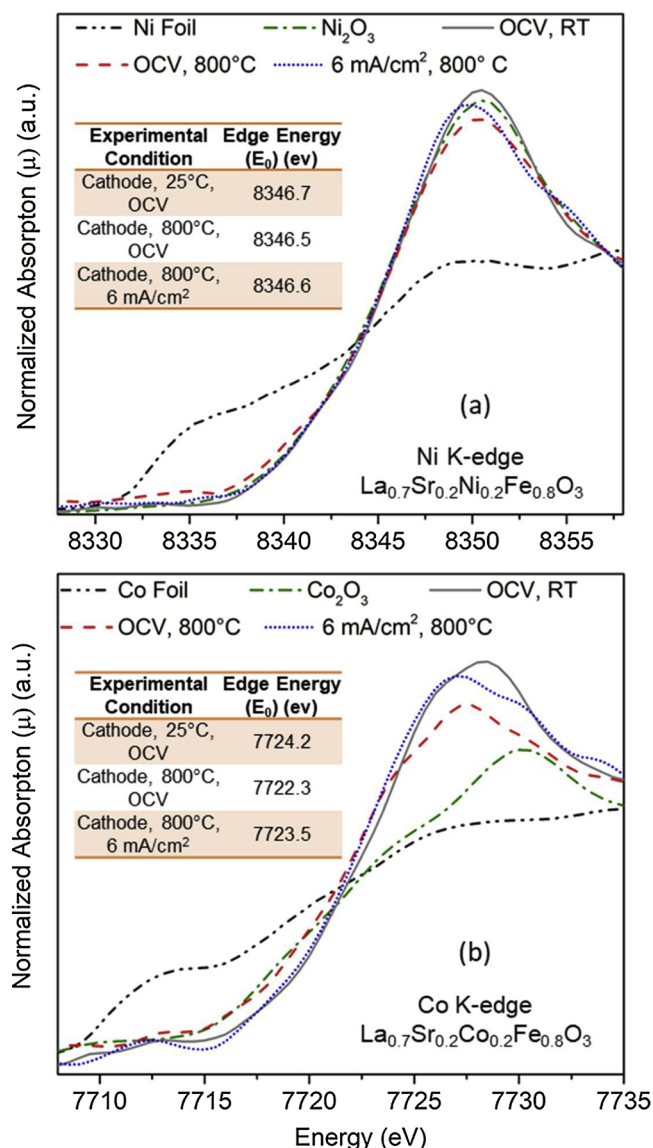


Fig. 8. (a) In-situ Ni K-edge XANES of $\text{La}_{0.7}\text{Sr}_{0.2}\text{Ni}_{0.2}\text{Fe}_{0.8}\text{O}_3$ cathode, and (b) In-situ Co K-edge XANES of $\text{La}_{0.7}\text{Sr}_{0.2}\text{Co}_{0.2}\text{Fe}_{0.8}\text{O}_3$ cathode collected under 40% CO_2 + 3% H_2O /He gas environment. Spectra were collected under OCV at both room temperature and 800 °C, and also under 6 mA/cm² electrolysis current density at 800 °C.

under 6 mA/cm² electrolysis current density at 800 °C in a CO_2 + H_2O /He environment. Similar to Fe K-edge of the sample, no significant shift was observed for Ni K-edge of $\text{La}_{0.7}\text{Sr}_{0.2}\text{Ni}_{0.2}\text{Fe}_{0.8}\text{O}_3$ cathode when the test conditions were changed (spectral resolution for Ni K-edge was 0.42 eV).

Fig. 8(b) shows the in-situ Co K-edge XANES of $\text{La}_{0.7}\text{Sr}_{0.2}\text{Co}_{0.2}\text{Fe}_{0.8}\text{O}_3$ cathode. Upon inspection of the near-edge region, it becomes clear that the edge energy shifts to a lower value when the cathode is heated from room temperature to 800 °C under OCV conditions in a CO_2 + H_2O /He gas environment. The edge energy values tabulated inside the figure gives a more quantitative verification of this visual observation. The edge energy of Co decreases from 7724.2 eV at room temperature to 7722.3 eV at 800 °C. The shift in this case is 1.9 eV, which is significantly higher than the Co K-edge spectral resolution of 0.38 eV in this beamline. Therefore, when the cell is heated, Co ions in $\text{La}_{0.7}\text{Sr}_{0.2}\text{Co}_{0.2}\text{Fe}_{0.8}\text{O}_3$ either reduces to a lower oxidation state or undergoes a change in the co-ordination number. It has already been reported in the literature that oxidation state of Co ions in the

doped ferrite-type perovskite oxides decreases with increase in temperature [97], and the change in XANES observed here may also be due to a partial reduction of the Co ions. Fig. 8(b) also shows the in-situ Co-Kedge XANES spectra of this cathode when an electrolysis current density of 6 mA/cm² was applied. It is observed that under current application, the XANES spectrum shifts to higher energy which may mean that cobalt ions attain a higher oxidation state. The edge energy under OCV at 800 °C is 7722.3 eV, while that under current application is 7723.5 eV, thereby yielding an edge energy shift of 1.2 eV towards higher energy, which may indicate an oxidation of the Co ions. This oxidation of Co ions can have an implication in the electrochemical activity of the $\text{La}_{0.7}\text{Sr}_{0.2}\text{Co}_{0.2}\text{Fe}_{0.8}\text{O}_3$ cathode for co-electrolysis. If the Co ions oxidize under electrolysis current, that would lead to a decrease in the number of oxygen vacancies to maintain charge neutrality in the material. Decrease in the number of oxygen vacancies will reduce the electrochemical activity of the cathode. Moreover, B-site ions are generally believed to be involved in the charge transfer process to the adsorbed reactive species [98,99]. As shown by earlier studies [18,41,100], activation of the cathode of such electrolysis cells take place by partial reduction of the B-site cation. Since Co ions may have been oxidized during co-electrolysis, some of the electrons supplied by external current might get consumed in lowering its oxidation state, which will in turn decrease Faradaic efficiency for syngas production.

3.9. DRIFTS during CO_2 + H_2O adsorption-desorption

To understand the relative strength of CO_2 and H_2O interactions with the surface of $\text{La}_{0.7}\text{Sr}_{0.2}\text{Co}_{0.2}\text{Fe}_{0.8}\text{O}_3$ and $\text{La}_{0.7}\text{Sr}_{0.2}\text{Ni}_{0.2}\text{Fe}_{0.8}\text{O}_3$, DRIFT spectra were collected during CO_2 + H_2O adsorption-desorption. CO_2 + H_2O was adsorbed at high temperature (450 °C was used as this is the highest temperature that the DRIFTS cell can reach) and then allowed to desorb at the same temperature. DRIFT spectra were then collected as a function of time (shown in Fig. 9). The bands at $\sim 1470\text{ cm}^{-1}$ for $\text{La}_{0.7}\text{Sr}_{0.2}\text{Co}_{0.2}\text{Fe}_{0.8}\text{O}_3$ and $\sim 1459\text{ cm}^{-1}$ for $\text{La}_{0.7}\text{Sr}_{0.2}\text{Ni}_{0.2}\text{Fe}_{0.8}\text{O}_3$ are due to adsorbed carbonate and bicarbonate species [101–103]. These are the intermediate reaction species that form on the cathode surface during the electrolysis operation. The doublets at 2364 cm^{-1} and 2332 cm^{-1} are due to molecularly adsorbed CO_2 . It is observed that the adsorbed CO_2 desorbs faster from the surface of $\text{La}_{0.7}\text{Sr}_{0.2}\text{Ni}_{0.2}\text{Fe}_{0.8}\text{O}_3$ than that of $\text{La}_{0.7}\text{Sr}_{0.2}\text{Co}_{0.2}\text{Fe}_{0.8}\text{O}_3$, indicating that the Co-doped sample has stronger surface interaction with CO_2 than the Ni-doped sample. This may be a reason behind the lower H_2/CO ratio obtained from $\text{La}_{0.7}\text{Sr}_{0.2}\text{Co}_{0.2}\text{Fe}_{0.8}\text{O}_3$ compared to $\text{La}_{0.7}\text{Sr}_{0.2}\text{Ni}_{0.2}\text{Fe}_{0.8}\text{O}_3$. However, too strong a bond with CO_2 might also lead to coke formation on $\text{La}_{0.7}\text{Sr}_{0.2}\text{Co}_{0.2}\text{Fe}_{0.8}\text{O}_3$ because the produced CO will not be able to desorb quickly. Following post-electrolysis treatment of cells shows that this indeed is the case.

3.10. Post-electrolysis analysis of cells: TPO and Raman spectroscopy

Cells containing $\text{La}_{0.7}\text{Sr}_{0.2}\text{Co}_{0.2}\text{Fe}_{0.8}\text{O}_3$ and $\text{La}_{0.7}\text{Sr}_{0.2}\text{Ni}_{0.2}\text{Fe}_{0.8}\text{O}_3$ cathodes were used to co-electrolyze 40% CO_2 + 3% H_2O /He at a current density of 3.5 mA/cm² for 24 h and the post-electrolysis cells were used to carry out a temperature-programmed oxidation (TPO) under 10% O_2 /He flow. Fig. 10 shows $m/z = 44$ mass-spectrometer signal generated by the TPO experiment. $\text{La}_{0.7}\text{Sr}_{0.2}\text{Co}_{0.2}\text{Fe}_{0.8}\text{O}_3$ cathode contains two types of carbon deposit on its surface: a less stable form of carbon indicated by the peaks at 345 °C and 462 °C, and more stable form of carbon such as the graphitic carbon [104,105] as indicated by the intense peak above 800 °C. On $\text{La}_{0.7}\text{Sr}_{0.2}\text{Ni}_{0.2}\text{Fe}_{0.8}\text{O}_3$ cathode, however, only the less stable carbon is seen. Raman spectra of the cathode side of these two post-electrolysis cells are also shown in the inset. As observed from Raman spectra, the Co-doped cathode shows D and G bands (1364 cm^{-1} and 1567 cm^{-1}) of carbonaceous species [105,106], whereas the Ni-doped cathode does not show these bands. The bands at 1250 cm^{-1} and 1370 cm^{-1} are related to the perovskite structure

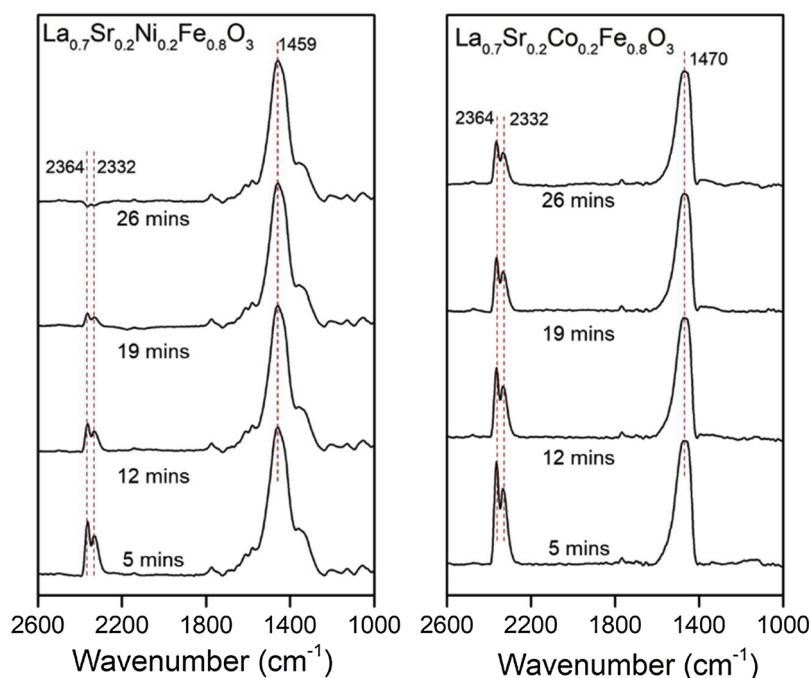


Fig. 9. DRIFTS spectra acquired over $\text{La}_{0.7}\text{Sr}_{0.2}\text{Ni}_{0.2}\text{Fe}_{0.8}\text{O}_3$ and $\text{La}_{0.7}\text{Sr}_{0.2}\text{Ni}_{0.2}\text{Fe}_{0.8}\text{O}_3$ powder during isothermal desorption (following adsorption of 40% CO_2 + 3% H_2O /He gas mixture at 450 °C) at different time intervals.

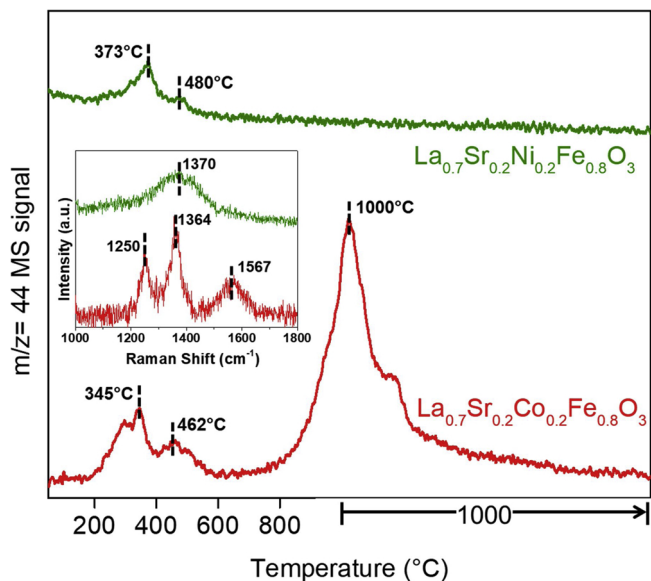


Fig. 10. Temperature-programmed oxidation of cells with $\text{La}_{0.7}\text{Sr}_{0.2}\text{Ni}_{0.2}\text{Fe}_{0.8}\text{O}_3$ and $\text{La}_{0.7}\text{Sr}_{0.2}\text{Ni}_{0.2}\text{Fe}_{0.8}\text{O}_3$ cathodes after CO_2 and H_2O co-electrolysis operation. Each cell was subjected to 3.5 mA/cm^2 electrolysis current density for 24 h in a 40% CO_2 + 3% H_2O /He environment at 800 °C before these post-reaction analyses. Inset shows Raman spectra of the cathode side of the same cells.

[65,107]. Thus, it can be said that Ni-doped sample has more resistance towards coking compared to the Co-doped sample. Since, the Co-doped sample reduces CO_2 all the way to carbon, it also shows lower Faradaic efficiency for syngas production as discussed in section 3.7. It will be shown later in section 3.13 that when both Ni and Co are present in the cathode, graphitic carbon deposition is not observed.

3.11. I–V curves and EIS of the cells during co-electrolysis operation

Fig. 11 shows the voltage vs current density behavior of the solid

oxide cells under 40% CO_2 /He and 40% CO_2 + 3% H_2O /He environments. When CO_2 and H_2O are fed into the cathode chamber without any reducing gas (CO or H_2), the open circuit voltage of the cell is determined by the oxygen partial pressure gradient between the anode and cathode sides [108,109]. Assuming the partial pressure of oxygen to be 0.21 on the anode side air, and 10^{-5} on the cathode side gas mixture (since the CO_2 cylinder had 0.001% oxygen as impurity), the OCV calculated by the Nernst equation at 800 °C is 0.23 V. The experimental OCV values in both CO_2 and CO_2 + H_2O gaseous environments are between 0.15 V to 0.2 V. OCV values of 0.1 V and even lower have been reported in the literature for electrolysis cells containing CO_2 at the cathode and air at the anode [108–111]. The small difference obtained in the OCV between the experimental and calculated values might be because of possible inaccuracies reported for the oxygen impurity in the CO_2 . The I–V curves show steep increase in cell voltages at low current density. CO_2 and H_2O reduction takes place beyond an onset potential and negligible current flow is realized until that onset potential is reached. This is the reason for the abrupt rise in cell voltage at low current density values [108–110,112]. Onset potential could be a function of the cathode material used, operating temperature as well as the cathode gas environment. Onset potentials in the range 0.7 V–1.0 V has been reported for CO_2 electrolysis [108–110,112]. This potential is found to be 0.8 V–0.9 V in this study. At voltages beyond this threshold value, current density is observed to be following an exponential behavior. For each of the solid oxide cells, voltage for CO_2 reduction process is seen to be higher than the voltage for co-electrolysis process. Thus, addition of water improves the electrocatalytic performance of the cells. A similar observation of higher cell voltage for dry CO_2 electrolysis compared to that for wet CO_2 electrolysis has been reported in the literature [29,32]. The cell with the Ni-doped $\text{La}_{0.7}\text{Sr}_{0.2}\text{Ni}_{0.2}\text{Fe}_{0.8}\text{O}_3$ cathode shows a larger difference between the cell voltages for dry and wet CO_2 electrolysis, possibly because the activity of this cathode is much higher for H_2O reduction than CO_2 reduction which is evident from the higher H_2 /CO ratio in the produced syngas.

Fig. 12(a) and (b) show the potentiostatic electrochemical impedance spectra of the electrolysis cells at OCV conditions under CO_2 and CO_2 + H_2O cathode environments, respectively. In both figures, the

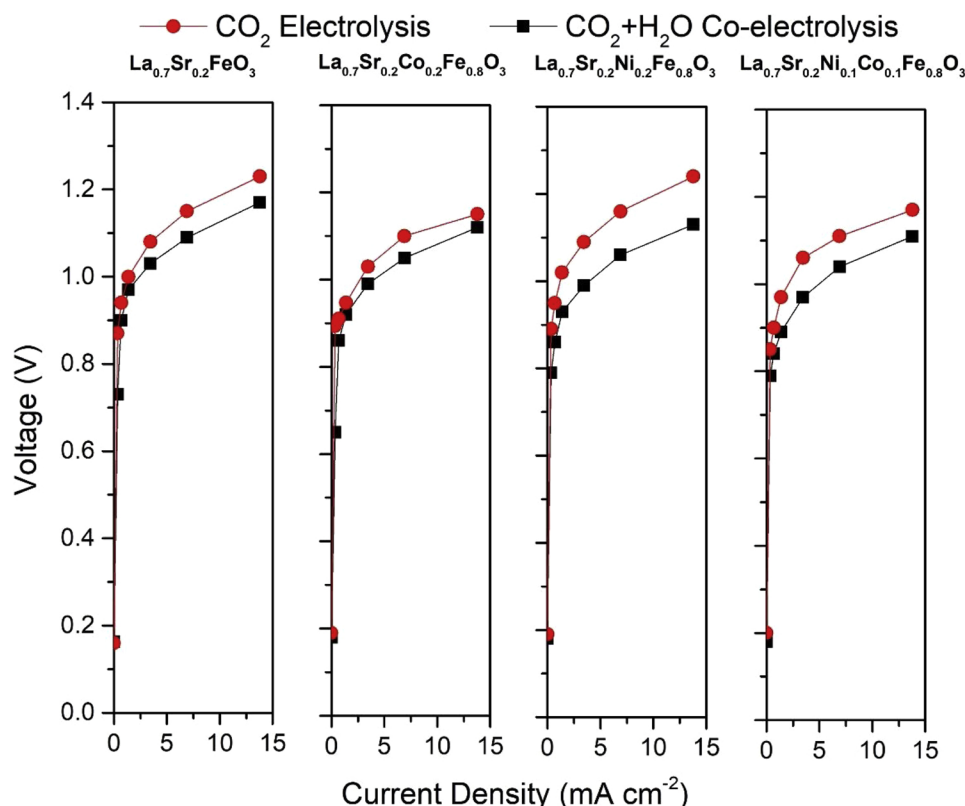


Fig. 11. I–V curves of solid oxide electrolysis cells containing ferrite cathodes, YSZ electrolyte and LSM-YSZ anode. Current density is under electrolysis operation with 40%CO₂ + 3%H₂O/He on the cathode side and air on the anode side at 800 °C.

insets show high frequency intercept of the impedance spectra, which corresponds to the total ohmic resistances of the cells. These ohmic resistances are in between 1.5 Ωcm² and 2.5 Ωcm². The calculated total ohmic resistance of the LSM-YSZ anode and ferrite perovskite cathode is lower than 0.01 Ωcm². However, assuming the ionic conductivity of YSZ at 800 °C to be 0.005 Scm^{−1} – 0.01 Scm^{−1} as reported in literature [113–115], an ohmic resistance of the YSZ electrolyte turns out to be 1.25–2.5 Ωcm² for a 125 μm thick electrolyte. Thus, the ohmic resistance of the cell is dominated by the resistance of the YSZ layer. Each of the EIS spectra in these two figures has two distinct features: a small high frequency arc and a large low frequency feature. The low frequency feature corresponds to resistance towards gas diffusion and

surface migration of the adsorbed and intermediate species [31,100,108,116,117], whereas the high frequency arc is typically a result of the activation resistance and concentration resistance of the electrodes. The linear high frequency feature in La_{0.7}Sr_{0.2}Ni_{0.2}Fe_{0.8}O₃ suggest the diffusion of reactants may be limiting the overall reaction at these frequencies under OCV. Thus, in these electrolysis cells, the dominant mode of overpotential loss under OCV is probably due to slower gas diffusion or surface migration of reactive species. Similar observations for steam electrolysis has been reported by Ishihara et al. [117] and Yue et al. [31], as well as for co-electrolysis by Li et al [116]. Fig. S7(a) and (b) shows the galvanostatic EIS collected at an electrolysis current of 0.7 mA/cm². It is observed that under applied bias, the

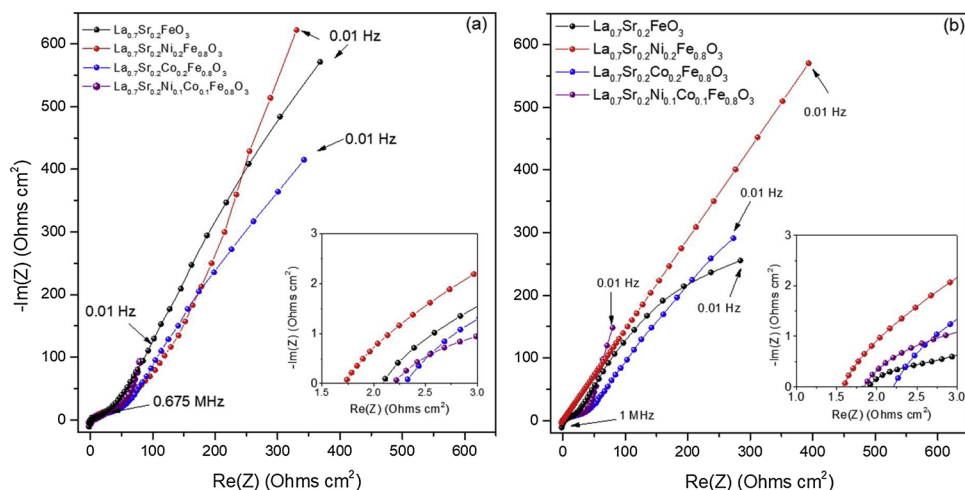


Fig. 12. Nyquist plots of EIS data collected at OCV from solid oxide electrolysis cells containing ferrite cathodes, YSZ electrolyte and LSM-YSZ anode at a temperature of 800 °C, flow of (a) 40%CO₂/He and (b) 40%CO₂ + 3%H₂O/He on the cathode side, and air the on anode side.

impedance of the cells decreases for both CO_2 and $\text{CO}_2 + \text{H}_2\text{O}$ electrolysis. This is due to the improved kinetics of adsorption/desorption as well as diffusion of the intermediate species to the triple phase boundary of the cathode during the electrolysis process.

3.12. Effect of inlet water concentration

The co-electrolysis of CO_2 and H_2O , results for which are shown in section 3.7, was performed on a 40% CO_2 + 3% H_2O /He feed mixture. In order to find the effect of varying feed composition on the electrochemical performance of the cells as well as on the H_2 /CO ratio of the produced syngas, co-electrolysis was performed on cathode feeds of 10 sccm 40% CO_2 + 10% H_2O /He and 40% CO_2 + 20% H_2O /He by employing a $\text{La}_{0.7}\text{Sr}_{0.2}\text{Ni}_{0.1}\text{Co}_{0.1}\text{Fe}_{0.8}\text{O}_3$ cathode. Table 5 summarizes the production rates and compositions of the syngas produced. Faradaic efficiencies of ~100% is observed for all the feed compositions. As the H_2O concentration in the feed increases from 3% to 10%, amount of H_2 produced increases, while CO amount decreases, hence increasing the H_2 /CO ratio. When the H_2O concentration in the feed is increased further to 20%, however, the H_2 /CO ratio of the produced syngas did not change anymore. Thus, even though initial increase of the H_2O concentration in the feed increases the H_2 /CO ratio of the syngas produced while maintaining high Faradaic efficiency, there seems to be an optimum ratio beyond which it will not increase with further increase in H_2O content in the feed.

Fig. 13 compares the current density vs voltage relationships during the co-electrolysis of feeds of various compositions. As also shown previously, cell voltage for electrolysis of dry 40% CO_2 /He is higher than that for co-electrolysis of 40% CO_2 + 3% H_2O /He at all the current densities. As the concentration of H_2O increases in the feed, the cell voltage decreases further. It has already been shown that increasing the H_2O content in the cathode feed does not significantly alter the Faradaic efficiency. Since increasing feed H_2O content decreases cell voltage, it can be said that it improves the electric power efficiency of the electrolysis cell.

3.13. Long term co-electrolysis test

In order to check the stability of the ferrite perovskites for co-electrolysis process, a long-term experiment was carried out for a duration of approximately 110 h using a 10 sccm feed stream containing 40% CO_2 + 10% H_2O /He at 800 °C and 7 mA/cm² electrolysis current density. $\text{La}_{0.7}\text{Sr}_{0.2}\text{Ni}_{0.1}\text{Co}_{0.1}\text{Fe}_{0.8}\text{O}_3$ was used as the representative cathode material in this experiment. Fig. 14 shows the cell voltage and the total Faradaic efficiency for production of H_2 and CO during the test period. The cell gives excellent Faradic efficiency (~100%) for the entire test duration, indicating stable long-term electrochemical performance. The cell voltage was 1.03 V at the beginning of the test, which increases to 1.07 V during the first 35 h and remains constant at this value for the rest of the experiment. Thus, the $\text{La}_{0.7}\text{Sr}_{0.2}\text{Ni}_{0.1}\text{Co}_{0.1}\text{Fe}_{0.8}\text{O}_3$ cathode undergoes little or no degradation during the long-term co-electrolysis process.

Table 5

Effect of inlet H_2O concentration on the production rates of H_2 and CO, H_2 /CO ratios, and Faradaic efficiencies during high temperature (800 °C) co-electrolysis of CO_2 and H_2O using a $\text{La}_{0.7}\text{Sr}_{0.2}\text{Ni}_{0.1}\text{Co}_{0.1}\text{Fe}_{0.8}\text{O}_3$ cathode.

Feed Composition	Production Rate (10 ⁴ mmol/cm ² /min) At 7 mA/cm ² , 800 °C		H_2 /CO Ratio	Faradaic Efficiency (± 10) (%)
	H_2	CO		
40% CO_2 + 3% H_2O /He	11.8	21.2	0.55	107
40% CO_2 + 10% H_2O /He	14.2	18.3	0.76	105
40% CO_2 + 20% H_2O /He	14.7	19.8	0.74	111

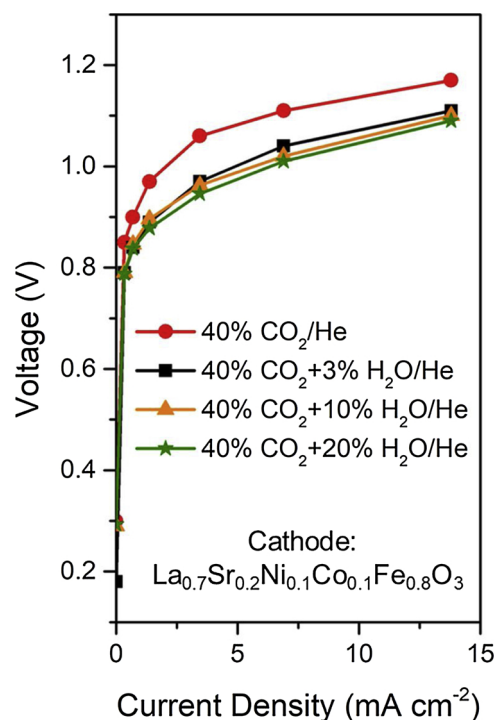


Fig. 13. I–V curve of an LSM-YSZ (anode)/YSZ/ $\text{La}_{0.7}\text{Sr}_{0.2}\text{Ni}_{0.1}\text{Co}_{0.1}\text{Fe}_{0.8}\text{O}_3$ (cathode) cell under 40% CO_2 and different H_2O concentrations on the cathode side at 800 °C in electrolysis mode.

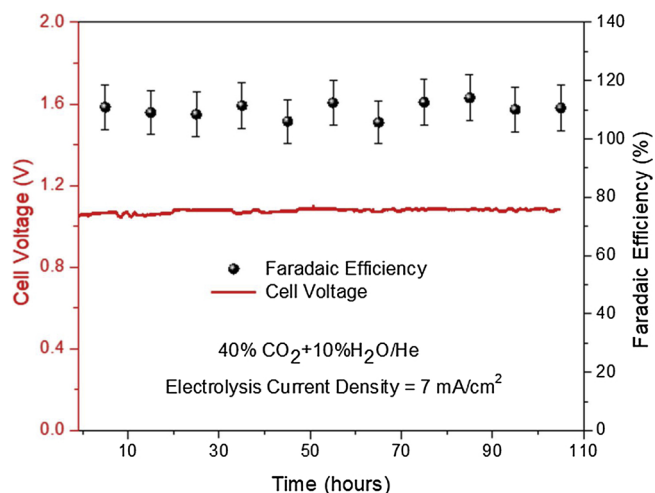


Fig. 14. Cell voltage and faradaic efficiency during a long-term co-electrolysis test with an LSM-YSZ (anode)/YSZ/ $\text{La}_{0.7}\text{Sr}_{0.2}\text{Ni}_{0.1}\text{Co}_{0.1}\text{Fe}_{0.8}\text{O}_3$ (cathode) cell at 800 °C using a cathode feed of 40% CO_2 + 10% H_2O /He.

Fig. S8 shows the Raman spectra of the $\text{La}_{0.7}\text{Sr}_{0.2}\text{Ni}_{0.1}\text{Co}_{0.1}\text{Fe}_{0.8}\text{O}_3$ cathode used in the long-term test before and after co-electrolysis. The spectra before reaction shows a band at 1330 cm^{-1} and the one after reaction shows a similar peak at 1360 cm^{-1} . Appearance of these bands are caused by A_g mode two phonon Raman scattering in the perovskite sample [65,107]. No features corresponding to D and G-bands (1350 cm^{-1} and 1580 cm^{-1} , respectively [106,118]) of carbonaceous materials can be observed in the Raman spectra of the cathode after co-electrolysis. This indicates that the Ni- and Co- doped ferrite perovskite cathodes have excellent resistance towards coke formation during co-electrolysis of CO_2 and H_2O .

4. Conclusions

In the current study, an A-site deficient perovskite $\text{La}_{0.7}\text{Sr}_{0.2}\text{FeO}_3$ was doped with Ni and Co at the B-site ($\text{La}_{0.7}\text{Sr}_{0.2}\text{Ni}_x\text{Co}_y\text{Fe}_{1-x-y}\text{O}_3$, ($x, y = 0$; $x = 0, y = 0.2$; $x = 0.1, y = 0.1$; $x = 0.2, y = 0$)) and was tested as cathode in a solid oxide electrolysis cell for CO_2 and H_2O co-electrolysis at 800 °C. Effect of such dopants on the material properties was also investigated using XRD, Raman spectroscopy, conductivity measurements, XPS, XANES, DRIFTS and temperature programmed treatments. The key findings are summarized below:

- 1) All the perovskite samples have orthorhombic phase symmetry except for $\text{La}_{0.7}\text{Sr}_{0.2}\text{Co}_{0.2}\text{Fe}_{0.8}\text{O}_3$ that has contributions from both orthorhombic and rhombohedral structures. The thermal expansion coefficient for Ni- doped samples are higher than B-site undoped or Co- doped samples. Ni and Co doping also changes the anion sublattice symmetry as seen from Raman spectroscopy.
- 2) Doping of the B-site with Ni and Co helps in improving the electrical conductivity and oxygen mobility of the samples. These ferrite perovskites are p-type conductors containing $\text{Fe}^{4+}/\text{Fe}^{3+}$, $\text{Ni}^{4+}/\text{Fe}^{3+}$ and $\text{Co}^{4+}/\text{Co}^{3+}$ charge carriers as shown by XPS and XANES.
- 3) Co-doping decreases the Faradaic efficiency for co-electrolysis of CO_2 and H_2O , because of coke formation as well as oxidation of Co ions under electrolysis conditions. However, efficiency increases to 100% on doping the samples with Ni. DRIFTS $\text{CO}_2 + \text{H}_2\text{O}$ adsorption-desorption experiments show that $\text{La}_{0.7}\text{Sr}_{0.2}\text{Co}_{0.2}\text{Fe}_{0.8}\text{O}_3$ interacts more strongly with CO_2 than $\text{La}_{0.7}\text{Sr}_{0.2}\text{Ni}_{0.2}\text{Fe}_{0.8}\text{O}_3$, which leads to lower H_2/CO ratio in the syngas produced by the Co- doped sample. H_2/CO ratio of the product syngas thus can be adjusted by tuning the Ni and Co content at the B-site of the cathode material. A long-term co-electrolysis test conducted for more than 100 h using $\text{La}_{0.7}\text{Sr}_{0.2}\text{Ni}_{0.1}\text{Co}_{0.1}\text{Fe}_{0.8}\text{O}_3$ cathode shows excellent stability of these materials under reaction conditions.

Acknowledgements

Financial support provided for this work by the U.S. Department of Energy, Office of Science, Office of Basic Energy Sciences under Award Number DE-FG02-07ER15896 is gratefully acknowledged.

The authors also acknowledge the assistance of Dr. Elizabeth Alexander (Surface Analysis Lab, The Ohio State University) on XPS. This research used resources of the Advanced Photon Source, a U.S. Department of Energy (DOE) Office of Science User Facility operated for the DOE Office of Science by Argonne National Laboratory under Contract No. DE-AC02-06CH11357. Assistance from the beamline scientists and staff of sector 10-BM beamline of Materials Research Collaborative Team (MRCAT) at the Advanced Photon Source is acknowledged.

Appendix A. Supplementary data

Supplementary material related to this article can be found, in the online version, at doi:<https://doi.org/10.1016/j.apcatb.2019.02.045>.

References

- [1] E.S.R. Laboratory, Global Monitoring Division, Trends in Atmospheric Carbon Dioxide, (2019).
- [2] G. Centi, S. Perathoner, Opportunities and prospects in the chemical recycling of carbon dioxide to fuels, *Catal. Today* 148 (2009) 191–205.
- [3] S. Uhm, Y.D. Kim, Electrochemical conversion of carbon dioxide in a solid oxide electrolysis cell, *Curr. Appl. Phys.* 14 (2014) 672–679.
- [4] L. Zhang, S. Hu, X. Zhu, W. Yang, Electrochemical reduction of CO_2 in solid oxide electrolysis cells, *J. Energy Chem.* 26 (2017) 593–601.
- [5] F. Alenazey, Y. Alyousef, O. Almisned, G. Almutairi, M. Ghouse, D. Montinaro, F. Ghigliazza, Production of synthesis gas (H_2 and CO) by high-temperature co-electrolysis of H_2O and CO_2 , *Int. J. Hydrogen Energy* 40 (2015) 10274–10280.
- [6] D.J. Cumming, A.R. Thompson, R.H. Rothman, Nickel impregnated cerium-doped

- strontium titanate fuel electrode: direct carbon dioxide electrolysis and Co-electrolysis, *J. Electrochem. Soc.* 163 (2016) F3057–F3061.
- [7] S.D. Ebbesen, C. Graves, M. Mogensen, Production of synthetic fuels by Co-electrolysis of steam and carbon dioxide, *Int. J. Green Energy* 6 (2009) 646–660.
- [8] L. Frost, E. Elangovan, J. Hartvigsen, Production of synthetic fuels by high-temperature co-electrolysis of carbon dioxide and steam with Fischer-Tropsch synthesis, *Can. J. Chem. Eng.* 94 (2016) 636–641.
- [9] C. Gaudillere, L. Navarrete, J.M. Serra, Syngas production at intermediate temperature through H_2O and CO_2 electrolysis with a Cu-based solid oxide electrolyzer cell, *Int. J. Hydrogen Energy* 39 (2014) 3047–3054.
- [10] C. Graves, S.D. Ebbesen, M. Mogensen, K.S. Lackner, Sustainable hydrocarbon fuels by recycling CO_2 and H_2O with renewable or nuclear energy, *Renew. Sustain. Energy Rev.* 15 (2011) 1–23.
- [11] P. Hjalmarsson, X. Sun, Y.L. Liu, M. Chen, Durability of high performance Ni–yttria stabilized zirconia supported solid oxide electrolysis cells at high current density, *J. Power Sources* 262 (2014) 316–322.
- [12] X. Hou, K. Zhao, J.-I. Yang, S. Ha, MoO_2 -based cathode for CO_2 and H_2O electrolysis, *Int. J. Hydrogen Energy* 41 (2016) 11895–11899.
- [13] E.T. Ioannidou, C.S. Neofytides, S.G. Neofytides, D.K. Niakolas, Modified NiO/GDC cermets as possible cathode electrocatalysts for H_2O electrolysis and $\text{H}_2\text{O}/\text{CO}_2$ Co-electrolysis processes in SOECs, *ECS Trans.* 78 (2017) 3267–3274.
- [14] T. Ishihara, S. Wang, K.-T. Wu, Highly active oxide cathode of $\text{La}(\text{Sr})\text{Fe}(\text{Mn})\text{O}_3$ for intermediate temperature CO_2 and $\text{CO}_2/\text{H}_2\text{O}$ co-electrolysis using LSGM electrolyte, *Solid State Ion.* 299 (2017) 60–63.
- [15] P. Kazempoor, R.J. Braun, Hydrogen and Synthetic Fuel Production Using High Temperature Solid Oxide Electrolysis Cells (SOECs), *Int. J. Hydrogen Energy* 40 (2015) 3599–3612.
- [16] S.-W. Kim, M. Park, H. Kim, K.J. Yoon, J.-W. Son, J.-H. Lee, B.-K. Kim, J.-H. Lee, J. Hong, In-situ nano-alloying Pd-Ni for economical control of syngas production from high-temperature thermo-electrochemical reduction of steam/ CO_2 , *Appl. Catal. B: Environ.* 200 (2017) 265–273.
- [17] W. Li, H. Wang, Y. Shi, N. Cai, Performance and methane production characteristics of $\text{H}_2\text{O}-\text{CO}_2$ co-electrolysis in solid oxide electrolysis cells, *Int. J. Hydrogen Energy* 38 (2013) 11104–11109.
- [18] Y. Li, P. Li, B. Hu, C. Xia, A nanostructured ceramic fuel electrode for efficient $\text{CO}_2/\text{H}_2\text{O}$ electrolysis without safe gas, *J. Mater. Chem. A* 4 (2016) 9236–9243.
- [19] C.K. Lim, Q. Liu, J. Zhou, Q. Sun, S.H. Chan, Sulfur tolerant LSCM-based composite cathode for high temperature electrolysis/Co-electrolysis of H_2O and CO_2 , *Fuel Cells* 17 (2017) 464–472.
- [20] M. Maide, K. Lillmaa, G. Nurk, E. Lust, Dependence of syngas composition on microstructure of $\text{La}_{0.8}\text{Sr}_{0.2}\text{Cr}_{0.5}\text{Mn}_{0.5}\text{O}_{3-\delta}$ based cathode for CO_2 and H_2O Co-electrolysis, *ECS Trans.* 78 (2017) 3275–3281.
- [21] M.T. Mehran, S.-B. Yu, D.-Y. Lee, J.-E. Hong, S.-B. Lee, S.-J. Park, R.-H. Song, T.-H. Lim, Production of syngas from $\text{H}_2\text{O}/\text{CO}_2$ by high-pressure coelectrolysis in tubular solid oxide cells, *Appl. Energy* 212 (2018) 759–770.
- [22] K.-M. Papazisi, D. Tsiplakides, S. Balomenou, High temperature Co-electrolysis of CO_2 and water on doped lanthanum chromites, *ECS Trans.* 78 (2017) 3197–3204.
- [23] C. Stoots, J. O'Brien, J. Hartvigsen, Results of recent high temperature coelectrolysis studies at the Idaho National Laboratory, *Int. J. Hydrogen Energy* 34 (2009) 4208–4215.
- [24] X. Sun, M. Chen, Y.L. Liu, P. Hjalmarsson, S.D. Ebbesen, S.H. Jensen, M. Mogensen, P.V. Hendriksen, Durability of solid oxide electrolysis cells for syngas production, *J. Electrochem. Soc.* 160 (2013) 1074–1080.
- [25] Y. Wang, T. Liu, S. Fang, F. Chen, Syngas production on a symmetrical solid oxide $\text{H}_2\text{O}/\text{CO}_2$ co-electrolysis cell with $\text{Sr}_2\text{Fe}_{1.5}\text{Mo}_{0.5}\text{O}_6-\text{Sm}_{0.2}\text{Ce}_{0.8}\text{O}_{1.9}$ electrodes, *J. Power Sources* 305 (2016) 240–248.
- [26] Y. Wang, T. Liu, L. Lei, F. Chen, High temperature solid oxide $\text{H}_2\text{O}/\text{CO}_2$ co-electrolysis for syngas production, *Fuel Process. Technol.* 161 (2017) 248–258.
- [27] R. Xing, Y. Wang, Y. Zhu, S. Liu, C. Jin, Co-electrolysis of steam and CO_2 in a solid oxide electrolysis cell with $\text{La}_{0.75}\text{Sr}_{0.25}\text{Cr}_{0.5}\text{Mn}_{0.5}\text{O}_{3-\delta}/\text{Cu}$ ceramic composite electrode, *J. Power Sources* 274 (2015) 260–264.
- [28] Y.-S. Yoo, S.-Y. Jeon, M.-A. Park, J. Lee, Y. Lee, Electrochemical performance of solid oxide electrolysis cells with LSCF6428-SDC/SDC electrode for $\text{H}_2\text{O}/\text{CO}_2$ high temperature Co-electrolysis, *ECS Trans.* 78 (2017) 3123–3128.
- [29] S.E. Yoon, S.H. Song, J. Choi, J.Y. Ahn, B.K. Kim, J.S. Park, Co-electrolysis of steam and CO_2 in a solid oxide electrolysis cell with ceramic composite electrodes, *Int. J. Hydrogen Energy* 39 (2014) 5497–5504.
- [30] S.-B. Yu, S.-H. Lee, M.T. Mehran, J.-E. Hong, J.-W. Lee, S.-B. Lee, S.-J. Park, R.-H. Song, J.-H. Shim, Y.-G. Shul, T.-H. Lim, Syngas production in high performing tubular solid oxide cells by using high-temperature $\text{H}_2\text{O}/\text{CO}_2$ co-electrolysis, *Chem. Eng. J.* 335 (2018) 41–51.
- [31] X. Yue, J.T.S. Irvine, $(\text{La},\text{Sr})(\text{Cr},\text{Mn})\text{O}_3/\text{GDC}$ cathode for high temperature steam electrolysis and steam-carbon dioxide co-electrolysis, *Solid State Ion.* 225 (2012) 131–135.
- [32] W. Zhang, Y. Zheng, B. Yu, J. Wang, J. Chen, Electrochemical characterization and mechanism analysis of high temperature Co-electrolysis of CO_2 and H_2O in a solid oxide electrolysis cell, *Int. J. Hydrogen Energy* (2017) 1–10.
- [33] X. Zhang, Y. Song, G. Wang, X. Bao, Co-electrolysis of CO_2 and H_2O in high-temperature solid oxide electrolysis cells: recent advance in cathodes, *J. Energy Chem.* (2017) 1–15.
- [34] Y. Zheng, J. Wang, B. Yu, W. Zhang, J. Chen, J. Qiao, J. Zhang, A review of high temperature co-electrolysis of H_2O and CO_2 to produce sustainable fuels using solid oxide electrolysis cells (SOECs): advanced materials and technology, *Chem. Soc. Rev.* 46 (2017) 1427–1463.
- [35] Y. Zheng, J. Zhou, L. Zhang, Q. Liu, Z. Pan, S.H. Chan, High-temperature electrolysis of simulated flue gas in solid oxide electrolysis cells, *Electrochim. Acta* 280

- (2018) 206–215.
- [36] S. Gunduz, D.J. Deka, U.S. Ozkan, Advances in High-temperature electrocatalytic reduction of CO₂ and H₂O, in: C. Song (Ed.), *Advances in Catalysis*, 6 Elsevier Academic Press, Cambridge, 2018, pp. 113–165.
 - [37] S. Gunduz, D. Dogu, D.J. Deka, K.E. Meyer, A. Fuller, A.C. Co, U.S. Ozkan, Application of solid electrolyte cells in ion pump and electrolyzer modes to promote catalytic reactions: an overview, *Catal. Today* 323 (2019) 3–13.
 - [38] V.N. Nguyen, L. Blum, Syngas and syngases from H₂O and CO₂: current status, *Chemie Ingenieur Tech.* 87 (2015) 354–375.
 - [39] C. Graves, S.D. Ebbesen, M. Mogensen, Co-electrolysis of CO₂ and H₂O in solid oxide cells: performance and durability, *Solid State Ion.* 192 (2011) 398–403.
 - [40] S.W. Kim, H. Kim, K.J. Yoon, J.H. Lee, B.K. Kim, W. Choi, J.H. Lee, J. Hong, Reactions and mass transport in high temperature co-electrolysis of Steam-CO₂ mixtures for syngas production, *J. Power Sources* 280 (2015) 630–639.
 - [41] K. Xie, Y. Zhang, G. Meng, J.T.S. Irvine, Direct synthesis of methane from CO₂/H₂O in an oxygen-ion conducting solid oxide electrolyser, *Energy Environ. Sci.* 4 (2011) 2218–2222.
 - [42] R.M. Ormerod, Solid oxide fuel cells, *Chem. Soc. Rev.* 32 (2003) 17–28.
 - [43] M.A. Pena, J.L.G. Fierro, Chemical structures and performance of perovskite oxides, *Chem. Rev.* 101 (2001) 1981–2017.
 - [44] R.J.H. Voorhoeve, D.W. Johnson, J.P. Remeika, P.K. Gallagher, Perovskite oxides: materials science in catalysis, *Science* 195 (1977) 827–833.
 - [45] X. Song, Z. Guo, Technologies for direct production of flexible H₂/CO synthesis gas, *Energy Convers. Manage.* 47 (2006) 560–569.
 - [46] B.H. Toby, R.B.V. Dreele, GSAS-II: the genesis of a modern open-source all purpose crystallography software package, *J. Appl. Crystallogr.* 46 (2013) 544–549.
 - [47] T.J.B. Holland, S.A.T. Redfern, Unit cell refinement from powder diffraction data: the use of regression diagnostics, *Mineral. Mag.* 61 (1997) 65–77.
 - [48] D. Dogu, K.E. Meyer, A. Fuller, S. Gunduz, D.J. Deka, N. Kramer, A.C. Co, U.S. Ozkan, Effect of lanthanum and chlorine doping on strontium titanates for the electrocatalytically-assisted oxidative dehydrogenation of ethane, *Appl. Catal. B: Environ.* 227 (2018) 90–101.
 - [49] B. Ravel, M. Newville, Athena, artemis, hephaestus: data analysis for X-ray absorption spectroscopy using IFEFFIT, *J. Synchrotron Radiat.* 12 (2005) 537–541.
 - [50] H. Falcon, A.E. Goeta, G. Punte, R.E. Carbonio, Crystal structure refinement and stability of LaFe_xNi_{1-x}O₃ solid solutions, *J. Solid State Chem.* 133 (1997) 379–385.
 - [51] M. Bevilacqua, T. Montini, C. Tavagnacco, G. Vicario, P. Fornasiero, M. Graziani, Influence of synthesis route on morphology and electrical properties of LaNi_{0.6}Fe_{0.4}O₃, *Solid State Ion.* 177 (2006) 2957–2965.
 - [52] N. Lakshminarayanan, H. Choi, J.N. Kuhn, U.S. Ozkan, Effect of additional B-site transition metal doping on oxygen transport and activation characteristics in La_{0.6}Sr_{0.4}(Co_{0.18}Fe_{0.72}X_{0.1})O_{3-δ} (where X = Zn, Ni or Cu) perovskite oxides, *Appl. Catal. B: Environ.* 103 (2011) 318–325.
 - [53] J.N. Kuhn, U.S. Ozkan, Effect of Co content upon the bulk structure of Sr- and Co-doped LaFeO₃, *Catal. Lett.* (2008) 179–188.
 - [54] T. Montini, M. Bevilacqua, E. Fonda, M.F. Casula, S. Lee, C. Tavagnacco, R.J. Gorte, P. Fornasiero, Relationship between electrical behavior and structural characteristics in Sr-Doped LaNi_{0.6}Fe_{0.4}O_{3-δ} mixed oxides, *Chem. Mater.* 21 (2009) 1768–1774.
 - [55] P. Lacroix, J.B. Torrance, J. Pannetier, S.A.I. Nazzari, P.W. Wang, T.C. Hunag, Synthesis, crystal structure, and properties of metallic PrNiO₃: comparison with metallic NdNiO₃ and semiconducting SmNiO₃, *J. Solid State Chem.* 91 (1991) 225–237.
 - [56] G.A. Maris, Structural Transitions Induced by Charge and Orbital Ordering in Transition Metal Oxides, University of Groningen, Groningen, 2004.
 - [57] R.D. Shannon, Revised effective ionic radii and systematic studies of interatomic distances in Halides and chalcogenides, *Acta Crystallogr. A* 32 (1976) 751–767.
 - [58] U. Holzwarth, N. Gibson, The Scherrer equation versus the ‘Debye-Scherrer equation’, *Nat. Nanotechnol.* 6 (2011) 534–535.
 - [59] G. Xiong, Z.-L. Zhi, X. Yang, L. Lu, X. Wang, Characterization of perovskite-type LaCoO₃ nanocrystals prepared by a stearic acid sol-gel process, *J. Mater. Sci. Lett.* 16 (1997) 1064–1068.
 - [60] W.Y. Hernandez, M.N. Tsampas, C. Zhao, A. Boreave, F. Bosset, P. Vernoux, La/Sr-based perovskites as soot oxidation catalysts for gasoline particulate filters, *Catal. Today* 258 (2015) 525–534.
 - [61] S.B. Adler, Chemical expansivity of electrochemical ceramics, *J. Am. Ceram. Soc.* 84 (2001) 2117–2119.
 - [62] M. Popa, J. Frantti, M. Kakihana, Characterization of LaMeO₃ (Me: Mn, Co, Fe) perovskite powders obtained by polymerizable complex method, *Solid State Ion.* 154–155 (2002) 135–141.
 - [63] E. Traversa, P. Nunziante, Synthesis and structural characterization of trimetallic perovskite-type rare-earth orthoferrites, La_xSm_{1-x}FeO₃, *J. Am. Ceram. Soc.* 83 (2000) 1087–1092.
 - [64] Y. Wang, J. Zhu, L. Zhang, X. Yang, L. Lu, X. Wang, Preparation and characterization of perovskite LaFeO₃ nanocrystals, *Mater. Lett.* 60 (2006) 1767–1770.
 - [65] G.S. Gallego, N.M. Alzate, O. Arnache, A novel LaFeO_{3-x}N_x oxynitride. Synthesis and characterization, *J. Alloys Compd.* 549 (2013) 163–169.
 - [66] G. Biasotto, A.Z. Simoes, C.R. Foschini, M.A. Zaghet, J.A. Varela, E. Longo, Microwave-hydrothermal synthesis of perovskite bismuth ferrite nanoparticles, *Mater. Res. Bull.* 46 (2011) 2543–2547.
 - [67] F.G. Garcia, C.S. Riccardi, A.Z. Simoes, Lanthanum doped BiFeO₃ powders: syntheses and characterization, *J. Alloys Compd.* 501 (2010) 25–29.
 - [68] G. Biasotto, A.Z. Simoes, C.R. Foschini, S.G. Antonio, M.A. Zaghet, J.A. Varela, A novel synthesis of perovskite bismuth ferrite nanoparticles, *Process. Appl. Ceram.* 5 (2011) 171–179.
 - [69] A.K. Opitz, A. Nanning, C. Rameshan, M. Kubicek, T. Gotsch, R. Blume, M. Havecker, A. Knop-Gericke, G. Rupprechter, B. Klötzer, J. Fleig, Surface chemistry of perovskite-type electrodes during high temperature CO₂ electrolysis investigated by operando photoelectron spectroscopy, *ACS Appl. Mater. Interfaces* 9 (2017) 35847–35860.
 - [70] Y. Teraoka, Y. Honbe, J. Ishii, H. Furukawa, I. Moriguchi, Catalytic effects in oxygen permeation through mixed-conductive LSCF perovskite membranes, *Solid State Ion.* 152–153 (2002) 681–687.
 - [71] N. Li, A. Boreave, J.-P. Deloume, F. Gaillard, Catalytic combustion of toluene over a Sr and Fe substituted LaCoO₃ perovskite, *Solid State Ion.* 179 (2008) 1396–1400.
 - [72] M. Alifanti, J. Kirchnerova, B. Delmon, D. Klvan, Methane and propane combustion over lanthanum transition-metal perovskites: role of oxygen mobility, *Appl. Catal. A: Gen.* (2004) 167–176.
 - [73] J.B. Pedley, E.M. Marshall, Thermochemical data for gaseous monoxides, *J. Phys. Chem. Ref. Data* 12 (1983) 967–1031.
 - [74] D.R. Lide, CRC Handbook of Chemistry and Physics, CRS Press, 2005.
 - [75] Y. Teraoka, M. Yoshimatsu, N. Yamazoe, T. Seiyama, Oxygen-sorptive properties and defect structure of perovskite-type oxides, *Chem. Lett.* (1984) 893–896.
 - [76] A. Longo, L.F. Liotta, D. Banerjee, V.L. Parola, F. Puleo, C. Cavallari, C.J. Sahle, M.M. Sala, A. Martorana, The effect of Ni doping on the performance and electronic structure of LSCF cathodes used for IT-SOFCs, *J. Phys. Chem. C* 122 (2018) 1003–1013.
 - [77] B. Wei, Z. Lu, X. Huang, M. Liu, N. Li, W. Su, Synthesis, electrical and electrochemical properties of Ba_{0.5}Sr_{0.5}Zn_{0.2}Fe_{0.8}O_{3-δ} perovskite oxide for IT-SOFC cathode, *J. Power Sources* 176 (2008) 1–8.
 - [78] Q. Ma, M. Balaguer, D. Perez-Coll, L.G.Jd. Haart, J.M. Serra, G.C. Mather, F. Tietz, N.H. Menzler, O. Guillon, Characterization and optimization of La_{0.97}Ni_{0.5}Co_{0.5}O_{3-δ}-Based air electrodes for solid oxide cells, *ACS Appl. Mater. Interfaces* 1 (2018) 2784–2792.
 - [79] K. Huang, H.Y. Lee, J.B. Goodenough, Sr- and Ni-Doped LaCoO₃ and LaFeO₃ perovskites, *J. Electrochem. Soc.* 145 (1998) 3220–3227.
 - [80] L.-W. Tai, M.M. Nasrallah, H.U. Anderson, D.M. Sparlin, S.R. Sehlin, Structure and electrical properties of La_{1-x}Sr_xCo_{1-y}Fe_yO₃, Part 1. The system La_{0.8}Sr_{0.2}Co_{1-y}Fe_yO₃, *Solid State Ion.* 76 (1995) 259–271.
 - [81] J.W. Stevenson, T.R. Armstrong, R.D. Carneim, L.R. Pederson, W.J. Weber, Electrochemical properties of mixed conducting perovskites La_{1-x}M_xCo_{1-y}Fe_yO_{3-δ} (M = Sr, Ba, Ca), *J. Electrochem. Soc.* 143 (1996) 2722–2729.
 - [82] Y. Liu, K. Chen, L. Zhao, B. Chi, J. Pu, S.P. Jiang, L. Jian, Performance stability and degradation mechanism of La_{0.6}Sr_{0.4}Co_{0.2}Fe_{0.8}O_{3-δ} cathodes under solid oxide fuel cells operation conditions, *Int. J. Hydrogen Energy* 39 (2014) 15868–15876.
 - [83] T. Tian, M. Zhan, W. Wang, C. Chen, Surface properties and catalytic performance in methane combustion of La_{0.7}Sr_{0.3}Fe_{1-y}Ga_yO_{3-δ} perovskite-type oxides, *Catal. Commun.* 10 (2009) 513–517.
 - [84] N.A. Merino, B.P. Barbero, P. Eloy, L.E. Cadus, La_{1-x}Ca_xCoO₃ perovskite-type oxides: identification of the surface oxygen species by XPS, *Appl. Surf. Sci.* 253 (2006) 1489–1493.
 - [85] K. Suththiporn, T. Maneerung, Y. Kathiraser, S. Kawi, CO₂ dry-reforming of methane over La_{0.8}Sr_{0.2}Ni_{0.8}Mo_{0.2}O₃ perovskite (M [Bi, Co, Cr, Cu, Fe]): roles of lattice oxygen on C-H activation and carbon suppression, *Int. J. Hydrogen Energy* 37 (2012) 11195–11207.
 - [86] Z. Zhao, H. Dai, J. Deng, Y. Du, Y. Liu, L. Zhang, Three-dimensionally ordered macroporous La_{0.6}Sr_{0.4}FeO_{3-δ} high-efficiency catalysts for the oxidative removal of toluene, *Microporous Mesoporous Mater.* 163 (2012) 131–139.
 - [87] B.J. Tan, K.J. Klabunde, P.M.A. Sherwood, XPS Studies of Solvated Metal Atom Dispersed Catalysts. Evidence for Layered Cobalt-Manganese Particles on Alumina and Silica, *J. Am. Chem. Soc.* 113 (1991) 855–861.
 - [88] R. Dudric, A. Vladescu, V. Rednic, M. Neumann, I.G. Deac, R. Tetea, XPS study on La_{0.67}Ca_{0.33}Mn_{1-x}Co_xO₃ compounds, *J. Mol. Struct.* 1073 (2014) 66–70.
 - [89] E.Y. Konyshova, M.V. Kuznetsov, Fluctuation of surface composition and chemical states at the hetero-interface in composites comprised of a phase with perovskite structure and a phase related to the Ruddlesden-Popper family of compounds, *RSC Adv.* 3 (2013) 14114–14122.
 - [90] R.H.Ev. Doorn, H.J.M. Bouwmeester, A.J. Burggraaf, Kinetic decomposition of La_{0.3}Sr_{0.7}CoO_{3-δ} perovskite membranes during oxygen permeation, *Solid State Ion.* 111 (1998) 263–272.
 - [91] K. Rida, A. Benabbas, F. Bouremmad, M.A. Pena, A. Martinez-Arias, Surface properties and catalytic performance of La_{1-x}Sr_xCrO₃ perovskite-type oxides for CO and C₃H₈ combustion, *Catal. Commun.* 7 (2006) 963–968.
 - [92] J.N. Kuhn, U.S. Ozkan, Surface properties of Sr- and Co-doped LaFeO₃, *J. Catal.* 253 (2008) 200–211.
 - [93] S. Maity, S.K. Ray, D. Bhattacharya, Phase, morphology and core-level electron spectroscopy of nano-sized La_{0.65}Sr_{0.35}MnO₃ powders prepared by solution combustion synthesis, *J. Phys. Chem. Solids* 74 (2013) 315–321.
 - [94] P.E.R. Blanchard, B.R. Slater, R.G. Cavell, A. Mar, A.P. Grosvenor, Electronic structure of lanthanum transition-metal oxyarsenides LaMAsO (M = Fe, Co, Ni) and LaFe_{1-x}M_xAsO (M' = Co, Ni) by X-ray photoelectron and absorption spectroscopy, *Solid State Sci.* 12 (2010) 50–58.
 - [95] J.F. Moulder, W.F. Stickle, P.E. Sobol, K.D. Bomben, Handbook of X-ray Photoelectron Spectroscopy, Perkin-Elmer Corporation, 1992.
 - [96] Y. Wang, T. Liu, S. Fang, F. Chen, Syngas production on a symmetrical solid oxide H₂O/CO₂ co-electrolysis cell with Sr₂Fe_{1.5}Mo_{0.5}O_{6-δ}-Sm_{0.2}Ce_{0.8}O_{1.9} electrodes, *J. Power Sources* 305 (2016) 240–248.
 - [97] A. Hagen, M.L. raulsen, W.-R. Kiebach, B.S. Johansen, Spectroelectrochemical cell for in situ studies of solid oxide fuel cells, *J. Synchrotron Radiat.* 19 (2012) 400–407.
 - [98] S. Liu, Q. Liu, J.-L. Luo, Highly stable and efficient catalyst with in situ exsolved Fe–Ni alloy nanospheres socketed on an oxygen deficient perovskite for direct

- CO₂ electrolysis, *ACS Catal.* 6 (2016) 6219–6228.
- [99] J. Suntivich, H.A. Gasteiger, N. Yabuuchi, H. Nakanishi, J.B. Goodenough, Y. Shao-Horn, Design principles for oxygen-reduction activity on perovskite oxide catalysts for fuel cells and metal–air batteries, *Nat. Chem.* 3 (2011) 546–550.
- [100] S. Xu, S. Li, W. Yao, D. Dong, K. Xie, Direct electrolysis of CO₂ using an oxygen-ion conducting solid oxide electrolyzer based on La_{0.75}Sr_{0.25}Cr_{0.5}Mn_{0.5}O_{3-δ} electrode, *J. Power Sources* 230 (2013) 115–121.
- [101] R. Philipp, K. Fujimoto, FTIR spectroscopic study of CO₂ adsorption/desorption on MgO/CaO catalysts, *J. Phys. Chem.* 96 (1992) 9035–9038.
- [102] A.A. Davydov, M.L. Shepotko, A.A. Budneva, Basic sites on the oxide surfaces: their effect on the catalytic methane coupling, *Catal. Today* 24 (1995) 225–230.
- [103] J.C. Lavalley, Infrared spectrometric studies of the surface basicity of metal oxides and zeolites using adsorbed probe molecules, *Catal. Today* 27 (1996) 377–401.
- [104] S.C. Fung, C.A. Querini, A highly sensitive detection method for temperature programmed oxidation of coke deposits: methanation of CO₂ in the presence of O₂, *J. Catal.* 138 (1992) 240–254.
- [105] I.H. Son, S.J. Lee, I.Y. Song, W.S. Jeon, I. Jung, D.J. Yun, D.-W. Jeong, J.-O. Shim, W.-J. Jang, H.-S. Roh, Study on coke formation over Ni/γ-Al₂O₃, Co-Ni/γ-Al₂O₃, and Mg-Co-Ni/γ-Al₂O₃ catalysts for carbon dioxide reforming of methane, *Fuel* 136 (2014) 194–200.
- [106] K. Mamtani, D. Jain, D. Zemlyanov, G. Celik, J. Luthman, G. Renkes, A.C. Co, U.S. Ozkan, Probing the oxygen reduction reaction active sites over nitrogen doped carbon nanostructures (CN_x) in acidic media using phosphate anion, *ACS Catal.* 6 (2016) 7249–7259.
- [107] M.K. Singh, H.M. Jang, H.C. Gupta, R.S. Katiyar, Polarized Raman scattering and lattice eigenmodes of antiferromagnetic NdFeO₃, *J. Raman Spectrosc.* 39 (2008) 842–848.
- [108] Y. Xie, J. Xiao, D. Liu, J. Liu, C. Yang, Electrolysis of carbon dioxide in a solid oxide electrolyzer with silver-gadolinium-doped ceria cathode, *J. Electrochem. Soc.* 162 (2015) F397–F402.
- [109] C. Ruan, K. Xie, A redox-stable chromate cathode decorated with in situ grown nickel nanocatalyst for efficient carbon dioxide electrolysis, *Catal. Sci. Technol.* 5 (2015) 19269–11940.
- [110] W. Qi, Y. Gan, D. Yin, Z. Li, G. Wu, K. Xie, Y. Wu, Remarkable chemical adsorption of manganedoped titanate for direct carbon dioxide electrolysis, *J. Mater. Chem. A* 2 (2014) 6904–6915.
- [111] Y. Tian, H. Zheng, L. Zhang, Bo Chi, J. Pu, J. Li, Direct electrolysis of CO₂ in symmetrical solid oxide electrolysis cell based on La_{0.6}Sr_{0.4}Fe_{0.8}Ni_{0.2}O_{3-δ} electrode, *J. Electrochem. Soc.* 165 (2018) F17–F23.
- [112] J.T.S. Irvine, C. Graves, D. Neagu, M.C. Verbraeken, C. Chatzichristodoulou, M.B. Mogensen, Evolution of the electrochemical interface in high-temperature fuel cells and electrolyzers, *Nat. Chem.* 1 (2016) 1–13.
- [113] R. Kungas, J.M. Vohs, R.J. Gorte, Effect of the ionic conductivity of the electrolyte in composite SOFC cathodes, *J. Electrochem. Soc.* 158 (2011) B743–B748.
- [114] C. Zhang, C.-J. Li, G. Zhang, X.-J. Ning, C.-X. Li, H. Liao, C. Coddet, Ionic conductivity and its temperature dependence of atmospheric plasma-sprayed yttria stabilized zirconia electrolyte, *Mater. Sci. Eng. B* 137 (2007) 24–30.
- [115] M. Han, X. Tang, H. Yin, S. Peng, Fabrication, microstructure and properties of a YSZ electrolyte for SOFCs, *J. Power Sources* 165 (2007) 757–763.
- [116] W. Li, H. Wang, Y. Shi, N. Cai, Performance and methane production characteristics of H₂O–CO₂ co-electrolysis in solid oxide electrolysis cells, *Int. J. Hydrogen Energy* 38 (2013).
- [117] T. Ishihara, N. Jirathiwathanakul, H. Zhong, Intermediate temperature solid oxide electrolysis cell using LaGaO₃ based perovskite electrolyte, *Energy Environ. Sci.* 3 (2010) 665–672.
- [118] I.H. Son, S.J. Lee, I.Y. Song, W.S. Jeon, I. Jung, D.J. Yun, D.-W. Jeong, J.-O. Shim, W.-J. Jang, H.-S. Roh, Study on coke formation over Ni/γ-Al₂O₃, Co-Ni/γ-Al₂O₃, and Mg-Co-Ni/γ-Al₂O₃ catalysts for carbon dioxide reforming of methane, *Fuel Cells* 136 (2014) 194–200.